

# 1 **Geometry of the deep Calabrian subduction (Central Mediterranean** 2 **Sea) from wide-angle seismic data and 3-D gravity modeling.**

3

4 David Dellong<sup>1,4</sup>, Frauke Klingelhoefer<sup>1</sup>, Anke Dannowski<sup>2</sup>, Heidrun Kopp<sup>2,3</sup>, Shane Murphy<sup>1</sup>,  
5 David Graindorge<sup>4</sup>, Lucia Margheriti<sup>5</sup>, Milena Moretti<sup>5</sup>, Giovanni Barreca<sup>6</sup>, Luciano Scarfi<sup>7</sup>, Alina  
6 Polonia<sup>8</sup>, Marc-Andre Gutscher<sup>4</sup>

7

8 (1) Géosciences Marines, IFREMER, Centre de Brest, Plouzané, France, (2) GEOMAR, Kiel,  
9 Germany, (3) Christian Albrechts University, Kiel, Germany (4) UMR LGO, University of Western  
10 Brittany, Brest, France (5) Istituto Nazionale di Geofisica e Vulcanologia (INGV)- Centro  
11 Nazionale Terremoti, Rome, Italy (6) Dipartimento di Scienze Biologiche, Geologiche ed  
12 Ambientali, University of Catania, Catania, Italy (7) Istituto Nazionale di Geofisica e Vulcanologia  
13 (INGV)- Osservatorio Etneo, Catania, Italy (8) ISMAR CNR, Bologna, Italy

## 14 **Abstract**

15 The Calabrian subduction zone is one of the narrowest arcs on Earth and a key area to  
16 understand the geodynamic evolution of the Mediterranean and other marginal seas. Here in the  
17 Ionian Sea, the African plate subducts beneath Eurasia. Imaging the boundary between the  
18 downgoing slab and the upper plate along the Calabrian subduction zone is important for  
19 assessing the potential of the subduction zone to generate mega-thrust earthquakes and was the  
20 main objective of this study. Here we present and analyze the results from a 380 km long, wide-  
21 angle seismic profile spanning the complete subduction zone, from the deep Ionian Basin and  
22 the accretionary wedge to NE Sicily, with additional constraints offered by 3-D Gravity modeling  
23 and the analysis of earthquake hypocenters. The velocity model for the wide-angle seismic  
24 profile images thin oceanic crust throughout the basin. The Calabrian backstop extends  
25 underneath the accretionary wedge to about 100 km SE of the coast. The seismic model was  
26 extended in depth using earthquake hypocenters. The combined results indicate that the slab dip  
27 increases abruptly from 2-3° to 60-70° over a distance of  $\leq 50$  km underneath the Calabrian  
28 backstop. This abrupt steepening is likely related to the roll-back geodynamic evolution of the  
29 narrow Calabrian slab which shows great similarity to the shallow and deep geometry of the  
30 Gibraltar slab.

## 31 **Plain language abstract**

32 We investigate the deep crustal structure of southern Italy and the Central Mediterranean where  
33 some of the oldest oceanic crust on Earth is actively descending (subducting) into the earth's  
34 interior (Speranza et al., 2012). This process causes much of the moderate seismicity observed  
35 in this region and may be responsible for strong historical earthquakes as well (Gutscher et al.,  
36 2006). Deep seismic data recorded during a marine geophysical expedition performed in 2014,  
37 allow us to reconstruct the 3-D geometry of this subduction zone. Our data reveal a 1-4 km thick  
38 evaporitic (salt bearing) layer in the 13 km thick accretionary wedge. The thin underlying crust  
39 has characteristics of oceanic crust. The adjacent onshore domains (E Sicily and SW Calabria)  
40 are composed of 25-30 km thick crust with velocities typical of continental crust. Together with  
41 earthquake travel-time tomography (providing images of the subducting slab down to 300 km)  
42 and gravity modeling we can for the first time image the abrupt steepening of the subducting  
43 slab, the "slab hinge", where slab dip increases from  $\leq 5^\circ$  to  $>60^\circ$  over a downdip distance of 50  
44 km. This slab dip is steep compared to other subduction zones, for example in Northern Honshu  
45 Japan or Sumatra, where the slab dip remains roughly  $10^\circ$  down to 40 km depth and therefore  
46 may have consequences on the seismicity of the region.

## 47 **1 Introduction**

48

49 The Calabrian arc is one of the narrowest subduction zones in the world. Here, the African plate  
50 subducts towards the NW beneath the Calabrian and Peloritan continental blocks. The forearc  
51 region is characterized by moderate seismicity with rare strong events (Scarfi et al., 2013;  
52 Carminati et al., 2005). Southern Italy has repeatedly been struck by strong earthquakes that  
53 also triggered tsunamis (e.g. Messina M7.1 in 1908; Hyblean earthquake M7.5 1693 - Piatanesi &  
54 Tinti, 1998; Jacques et al., 2001; Gutscher et al., 2006). The seismicity of the slab is distributed  
55 along a well-defined Wadati-Benioff zone with focal depth that are less than 50 km in the Ionian  
56 basin and down to 660 km in the Tyrrhenian Basin (Engdahl et al., 1998; Selvaggi & Chiarabba,  
57 1995).

58

59 Imaging the boundary between the downgoing slab and the upper plate along the Calabrian  
60 subduction zone is important for assessing the potential of a subduction zone to create mega-  
61 thrust earthquakes. Indeed, many authors consider that earthquake rupture cannot extend  
62 beyond the intersection with the mantle wedge, which is thought to be highly serpentized  
63 (Byrne et al., 1988; Oleskevich et al., 1999). Other workers have hypothesized that there is a  
64 significant influx of hot mantle beneath Calabria (Westaway, 1993; Ferranti et al., 2007) and  
65 others evoke slab break-off and possible delamination beneath central E Sicily and Calabria  
66 (Piana Agostinetti et al., 2009; Faccenna et al., 2011; Giacomuzzi et al., 2012). However, the  
67 exact depth and dip of the downgoing slab, as well as the thickness and nature of the upper plate  
68 (Calabria block) remain uncertain. This study tries to unravel the slab geometry and the slab  
69 depth in the Calabrian subduction zone using wide-angle seismic data and gravity modeling as  
70 well as earthquake locations and regional tomographic data.

71

### 72 **1.1 Tectonic history of the study region**

73 The evolution of the central western Mediterranean region is driven by the convergence  
74 between the African plate and the Iberian and Eurasian plates leading to subduction  
75 initiation, slab rollback and the formation of back-arc basins (Faccenna et al., 2011;  
76 Rosenbaum et al., 2002; Handy et al., 2010; van Hinsbergen et al., 2014a; Jolivet et al.,  
77 2015) (Figure 1). NW dipping subduction and ensuing rollback is thought to have started at  
78 35-30 Ma (Rosenbaum et al., 2002; van Hinsbergen et al., 2014a). At 25 Ma the Sardinia-  
79 Corsica block began rotating in a counter-clockwise direction in response to SE-ward retreat  
80 of the subduction (Rosenbaum et al., 2002). This led to widespread extension causing the  
81 opening of the Liguro-Provençal and Valencia basins (Séranne, 1999). The original forearc  
82 then split into individual blocks known as AlKaPeCa (Alboran, Kabyliides, Peloritan, Calabria)  
83 continental terranes (Bouillin et al., 1986). The Calabrian slab rolled back to the E and the  
84 overriding continental blocks were thrust onto the margin of Adria forming the southern  
85 Apennines. The Peloritan block has overthrust the African margin of Sicily (Speranza et al.,  
86 2003). A slab length offset between the originally attached Calabrian and Kabyliides slab  
87 might be at the origin of the initiation of a STEP (Subduction Transform Edge Propagator,  
88 Govers & Wortel, 2005) fault that then separated these into two slabs (van Hinsbergen et al.,  
89 2014a). The modern day forearc STEP fault is thought to be located either at the Alfeo Fault  
90 system (Gutscher et al., 2016; 2017; Dellong et al., 2018) or at the Ionian Fault system  
91 (Polonia et al., 2011; Scarfi et al., 2018) (Figure 2). An earlier proposition that the STEP fault  
92 follows the Malta Escarpment, a 3-km high feature offshore E Sicily (Argnani and Bonazzi,  
93 2005) formed during the Tethyan rifting history of the Ionian Sea (Gallais et al., 2011; Frizon  
94 de Lamotte et al., 2011) seems unlikely given the absence of tectonic deformation along the  
95 central to southern Malta Escarpment since the Messinian, on the basis on high-resolution

96 seismic profiles shot across the escarpment (Gutscher et al., 2016).

## 97 **1.2 Deep structure of the Ionian basin and the Malta escarpment**

98 Several deep seismic reflection and refraction studies were conducted on the eastern Sicily  
99 margin in the 80's and 90's (Makris et al. 1986, Hirn et al. 1997, Nicolich et al. 2000,  
100 Catalano et al. 2001). These studies concluded that a 30 km thick continental crust underlies  
101 the Sicilian-Hyblean plateau. An Expanding Spread Profile (ESP) experiment located in the  
102 Ionian Abyssal Plain (IAP) and on the Mediterranean ridge provided the first constraints on  
103 the crustal velocities of the deep IAP, where the sedimentary cover is thinnest. The wide-  
104 angle seismic results show a 5 km thick sedimentary cover overlying a thin crust of about 7  
105 to 9 km (de Voogd et al. 1992, Le Meur 1997). However, different interpretations were  
106 proposed including a thinned continental crust or an oceanic one. Later studies clearly  
107 imaged a 5-6 km thick oceanic crust in the basin spanning the northern IAP (Dellong et al.,  
108 2018; Dannowski et al., 2019). Previous multi-channel seismic (MCS) studies have imaged  
109 the deep structure of the Ionian Basin and the adjacent Calabrian accretionary wedge, with  
110 sediment thicknesses increasing from about 5 km (undeformed thickness) in the abyssal  
111 plain to 10-15 km within the accretionary wedge as the dip of the subducting plate below  
112 remains very shallow (1-2° on average) (Cernobori et al., 1996; Minelli and Faccenna, 2010;  
113 Polonia et al., 2011; Gallais et al., 2011; Maesano et al., 2017). An early MCS study imaged  
114 the steepening of the subducting basement as it approaches the Calabrian block (lines ION-  
115 3 and ION-4) (Cernobori et al., 1996). At the transition between the continental (Sicilian) and  
116 the deep oceanic (Ionian) domain an abrupt crustal thinning by 3km is observed along the  
117 Malta Escarpment. The escarpment was originally interpreted to be a passive margin  
118 originating from the initial opening of the Ionian Sea. Later studies proposed this to be a  
119 transform margin (Frizon de Lamotte, 2011; Gallais et al., 2011; Dellong et al., 2018,  
120 Catalano et al., 2001) which is in good agreement with an opening at the Late Triassic/Early  
121 Jurassic of the Ionian Basin (Frizon de Lamotte, 2011). Other studies propose ages ranging  
122 from Early Late Triassic (220 Ma; Speranza et al., 2012) to Late Jurassic to Early  
123 Cretaceous (Catalano et al., 2001).

124

125 Travel time tomography using local or teleseismic events has been able to image downgoing  
126 slabs in subduction zones to depth of several hundreds of kilometers (eg. Spakman et al.,  
127 1993, Spakman & Wortel, 2004, Wortel & Spakman, 2000). One of the first studies of the  
128 Italian region showed large-scale lithospheric inhomogeneity in the deep structure of the  
129 Tyrrhenian Sea (Scarpa, 1982). Positive travel-time anomalies interpreted to be a NW  
130 dipping subducting slab beneath the Calabrian arc were later imaged from teleseismic  
131 events (Amato et al., 1993). Results from 3-D teleseismic tomography focussed on the study  
132 region reveal the downgoing slab as a fast structure extending 350 km laterally from  
133 northern Sicily to southern Campania and 400 km vertically (Cimini, 1999). A more refined  
134 mantle tomography imaged a 150-km wide slab window beneath the southern Apennines  
135 which probably opened after a slab tear occurred between the Apulian continental  
136 subduction and the Ionian oceanic slab (Chiarabba et al., 2008). These results were refined  
137 using a denser data set and led to the proposition that the subducting lithosphere remains  
138 attached along a 100-km-long segment at the central portion of the Calabrian arc (Neri et al.,  
139 2012). Global tomography models clearly image a horizontal anomaly in the transition zone  
140 at a depth of 500 km, which is interpreted to be a flat lying part of the Calabrian slab  
141 (Spakman & Wortel, 2004, Wortel & Spakman, 2000). The existence of a proposed STEP  
142 fault (Govers & Wortel, 2005, Wortel et al., 2009) was confirmed by tomographic and gravity  
143 modeling, with a proposed location of the faults in the Tindari and Crotona Basin (Neri et al.,  
144 2012, Figure 1 for location). Recent geodetic work provided evidence for toroidal flow around

145 the retreating slab edges of the Calabrian subduction system expressed by counter-  
146 clockwise rotations at the northern and clockwise rotations at the southern edge of the slab  
147 corresponding to movements predicted by STEP faults (Palano et al., 2017). Recent  
148 tomographic studies imaged a trench-parallel slab break-off on both sides of the slab which  
149 might be still propagating, narrowing the slab. (Barreca et al., 2016; 2018; Scarfi et al., 2016;  
150 2018). Horizontal tearing affecting both sides of the slab was proposed to result in a  
151 narrowing of the subduction system and enhanced subsidence along the still intact segment  
152 of the slab (Scarfi et al., 2018). In central Calabria the depth of the slab has been determined  
153 by source-receiver function analysis during the CAT/SCAN experiment. The results show  
154 that the slab is steeply inclined and a 4-6 km thick layer of low-velocity sediments is imaged  
155 between the oceanic crust and the continental Calabrian backstop (Piana Agostinetti et al.,  
156 2009).

157

158 Gravity anomalies at subduction zones are generally characterized by strong signatures that  
159 are linked to topographic effects, material density and temperature heterogeneities in the  
160 lithospheric mantle and the crust, or even forces and stresses induced by plate dynamics  
161 (eg. Levit and Sandwell, 1995; Krien and Fleitout, 2008 and references therein). Gravity  
162 anomaly lineaments parallel to the arc-trench axis are often observed along subduction  
163 zones. For example, a negative free-air anomaly is usually observed at the trench and above  
164 the downgoing slab, and is interpreted as a result of a topographic effect, or of the presence  
165 of a light crustal material entrapped within the subduction complex (Forte et al. 1993;  
166 Marotta et al., 2006). It was suggested that great earthquakes occur predominantly in  
167 regions with a strongly negative trench-parallel gravity anomaly (Song and Simons, 2003).  
168 Earlier studies in the Ionian sea have shown that Bouguer gravity anomalies are consistent  
169 with young subduction of an intermediate foreland lithosphere beneath two opposing  
170 subduction systems, the Apennine-Calabrian system to the SW, and the Hellenic system to  
171 the northeast (Moretti and Royden, 1988).

172

173 Determining the position of the slab at shallow depth compared to earthquake tomographic  
174 studies and using seismic and gravimetry methods remains difficult because of the thick  
175 accretionary wedge and the Messinian evaporites layers introducing velocity inversions and  
176 density anomalies. This study aims to shed light on the deep structure of the Ionian  
177 subduction interface below the Calabro-Peloritan backstop with a higher resolution than the  
178 above mentioned tomography and receiver function studies.

179

### 180 **1.3 Objectives of the study**

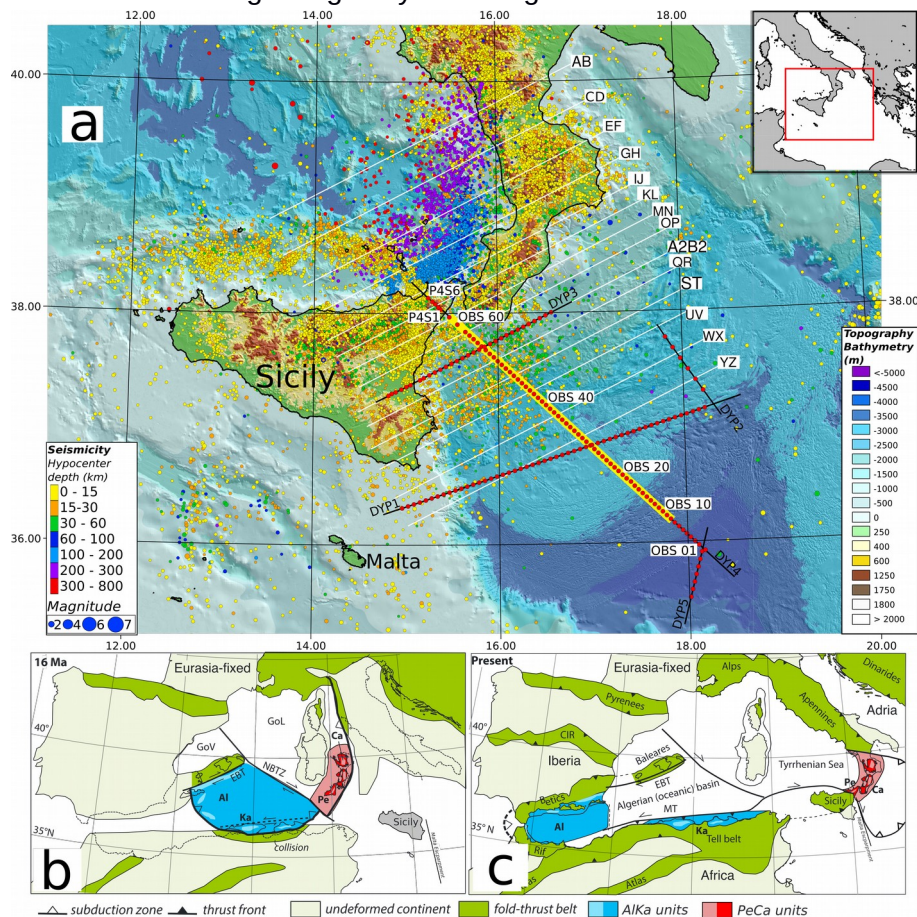
181 Four wide-angle seismic profiles were acquired to provide a 3-D image of the ESicily margin  
182 and the western portion of the Calabrian subduction zone (Figures 1 and 2). Two profiles  
183 orthogonal to the E Sicily margin cross the Malta Escarpment and the transition between  
184 continental crust of the Hyblean plateau - and the Tethyan oceanic crust of the deep Ionian  
185 basin (Dellong et al., 2018). One profile close to the Medina seamounts was shot to  
186 characterize the nature of the crust below the Ionian Abyssal Plain (Dannowski et al., 2019).  
187 Our work presents the findings of the 380 km long dip line, intersecting the three other  
188 profiles, and thus provides a comprehensive 3-D structural view of the analysed sector. The  
189 dip line crosses from the undeformed domain of the Ionian Abyssal Plain, across the external  
190 (evaporitic) Calabrian accretionary complex, the internal (clastic) accretionary wedge, and all  
191 the way to the Peloritan continental domain (NE corner of Sicily), composed of Hercynian  
192 metamorphic basement currently forming the backstop of the upper plate. The objective of  
193 this combined data set is to image the complex 3-D transition between the adjacent and



194 overlapping crustal domains, as well as the deep expression of the lateral slab tear (STEP)  
 195 fault. Among the open questions which remained following the previously published work are  
 196 (eg. Dellong et al., 2018): what is the geometry (depth, thickness, dip) of the downgoing  
 197 oceanic crust and its relative position to the overlying backstop? How does the thickness and  
 198 nature of the accreted and/or underplated sediments vary downdip? We analyze the first  
 199 wide-angle seismic data compilation that can address this set of questions.

200

201 Furthermore, regional 3-D gravity modeling was performed with the aim to test end-member  
 202 models for the slab depth in the Calabrian - Messina strait region. Specifically, in wide-angle  
 203 profile DY-P3, the top of the subducting oceanic crust was not imaged (Dellong et al., 2018).  
 204 The authors proposed two hypotheses for its position (1) significantly below the Calabrian  
 205 backstop and beyond the range of the seismic rays; (2) or that the slab is part of the thick  
 206 lower crustal layer of the backstop but not resolved by the OBS data given that velocity  
 207 contrasts would be minor producing no high amplitude reflection. As an intervening layer with  
 208 mantle velocities (first hypothesis) will produce a strong, observable gravity anomaly this  
 209 problem can be resolved using 3-D gravity modeling.



211 *Figure 1: (a) Location map of the study area. Ocean bottom seismometers and landstations*  
 212 *deployed during the Dionysus cruise (Oct.-Nov. 2014, Meteor).. Earthquakes from the INGV-*  
 213 *ISIDe catalogue (<http://cnt.rm.ingv.it/en>) are plotted with a size proportional to the magnitude*  
 214 *and color corresponding to the hypocenter depth. The CROP-M3 MCS profile is coincident*  
 215 *with DY-P4 and marked by underlying bold yellow line (Figure 5 this study and shown in*  
 216 *detail in Polonia et al., 2011). Profiles used for the construction of the gravity model are*  
 217 *marked by white lines. Bathymetry from Gutscher et al., 2017 and EMODNET. (b) and (c)*  
 218 *Paleogeographic reconstruction figures are modified from van Hinsbergen et al., 2014a. Al =*

219 *Alboran*; *Ca* = Calabria; *CIR* = Central Iberian Ranges; *EBT* = Emile Baudot Transform; *GoL*  
220 = Gulf of Lion; *GoV* = Gulf of Valencia; *Ka* = Kabylides; *NBTZ* = North Balearic Transform  
221 Zone; *Pe* = Peloritian Mountains. Inset shows the location of the study area in the central  
222 Mediterranean region.

## 223 **2 Data acquisition and processing**

224 The wide-angle seismic data were acquired in 2014 during the Dionysus survey, a  
225 collaboration between Geomar (Kiel, Germany), INGV (Rome, Italy), Ifremer and the  
226 University of Brest (both Brest, France) onboard the R/V Meteor (M111 cruise). Additionally,  
227 we used gravity data from satellite free-air anomaly from the World Gravity Map (WGM-2012  
228 – Bonvalot et al., 2012; Pavlis et al., 2012) for gravity modeling.

### 229 **2.1 Wide-angle seismic data**

230 Three long and one shorter wide-angle seismic profiles were shot using an array of six GI-  
231 Guns of a total volume of 84 liters (5,440 in<sup>3</sup>) (Figure 2). This work focuses on the DY-P4  
232 profile which spans the Calabrian subduction zone along a SE-NW transect.

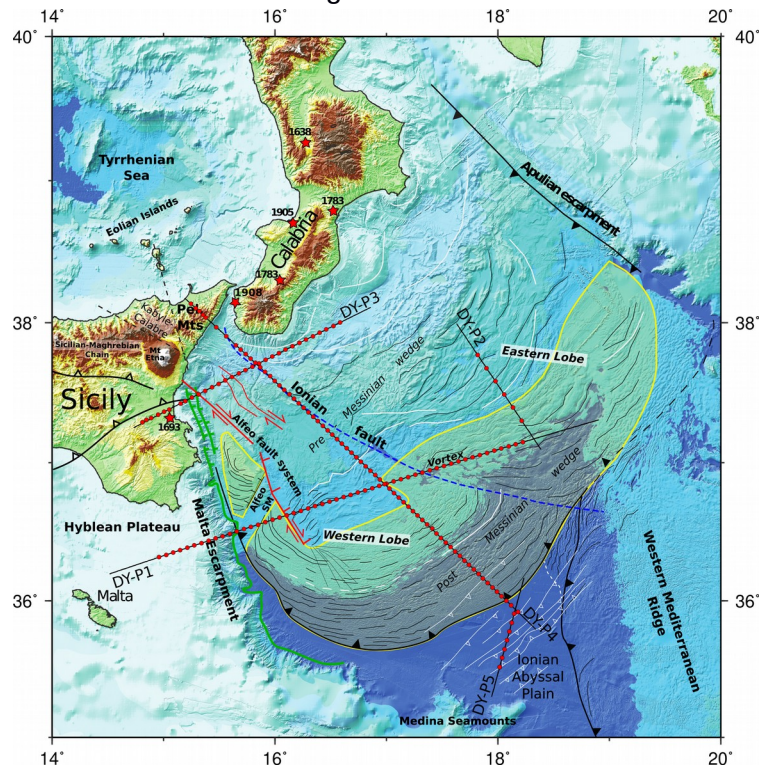
233

234 Half of the marine instruments used in this experiment were MicroOBS from Ifremer equipped  
235 with three-component 4.5 Hz geophones and a hydrophone both recording at a 4 ms  
236 sampling rate (Auffret et al., 2004). The other half consisted of OBH (Ocean Bottom  
237 Hydrophones) from Geomar (Bialas & Flueh, 1999). OBS were deployed on even position  
238 numbers and OBH on odd position numbers. The land stations were six REF TEK 130S-01  
239 equipped with short period velocimeter sensors with a 1 s dominant period. Their sampling  
240 rate was set at 8 ms. The seismic source used during the survey consisted of two subarrays  
241 of 6 GI-Guns. The 12 guns together provided a volume of 84 l (5,440 in<sup>3</sup>) and were operated  
242 at 190 bar. The shooting interval was set to a constant 60 s for all profiles, resulting in a shot  
243 point interval of 150 m. The marine part of the profile is co-incident with the deep reflection  
244 seismic profile CROP M2B which was used in this study to constrain the geometry of the  
245 sedimentary layers (Polonia et al., 2011) (Figures 1 and 5).

246 We installed 61 ocean bottom instruments along profile DY-P4 at 5-6 km intervals and 5  
247 INGV landstations in Sicily along the prolongation of the profiles (see Figure 2). Data quality  
248 is good, however, arrivals are highly distorted and energy is lost at long offsets probably due  
249 to the highly irregular sedimentary layer boundaries and the presence of salt leading to a  
250 velocity inversion in the sedimentary column (Figures 3 and supplementary materials Figure  
251 S1). The land-station data are of very good quality and reflections picked from the data  
252 sections were one of the main inputs for the modeling of the subducting oceanic plate  
253 geometry (Figure 4). Initial processing was performed onboard, and profiles DY-P1 and DY-  
254 P3 were modelled using a forward approach (Dellong et al., 2018). This study uses an  
255 identical approach for profile DY-P4 to achieve inter-comparable models. The OBS data  
256 were corrected for time and spatial drift during the deployment on board. First arrival time  
257 picking and a preliminary tomographic inversion were equally run on board, however the  
258 resulting preliminary velocity models showed high uncertainties, due to the velocity inversion  
259 of the salt layer and the low density of seismic rays reaching lower crustal and upper mantle  
260 depth. Because of these difficulties the data were modeled using the “*Rayinvr*” software (Zelt  
261 & Smith, 1992; Zelt, 1999) to be able to include additional information from coincident  
262 reflection seismic data and gravity modeling. This approach uses a combined forward and  
263 inversion approach to model layers of different velocities and velocities gradients. Layer  
264 depth and velocities are defined by the user in the first place. A smoothed inversion at  
265 velocity and depth nodes selected by the user can be used additionally to constrain the best



266 fitting solutions. Depending on the data quality either the hydrophone or the vertical  
267 geophone data were used for the modeling.



269 *Figure 2: Tectonic map of the study area. Ocean bottom seismometers and landstations are*  
270 *marked by red dots. Red stars mark hypocenters location of historical earthquakes. CROP-*  
271 *M3 MCS profile is coincident to DY-P4 (Figure 5; Polonia et al., 2011). Bathymetry from*  
272 *Gutscher et al., 2017. (After Dellong et al., 2018). Yellow shaded area marks the supposed*  
273 *extension of tectonically thickened evaporites in the Calabrian accretionary wedge.*

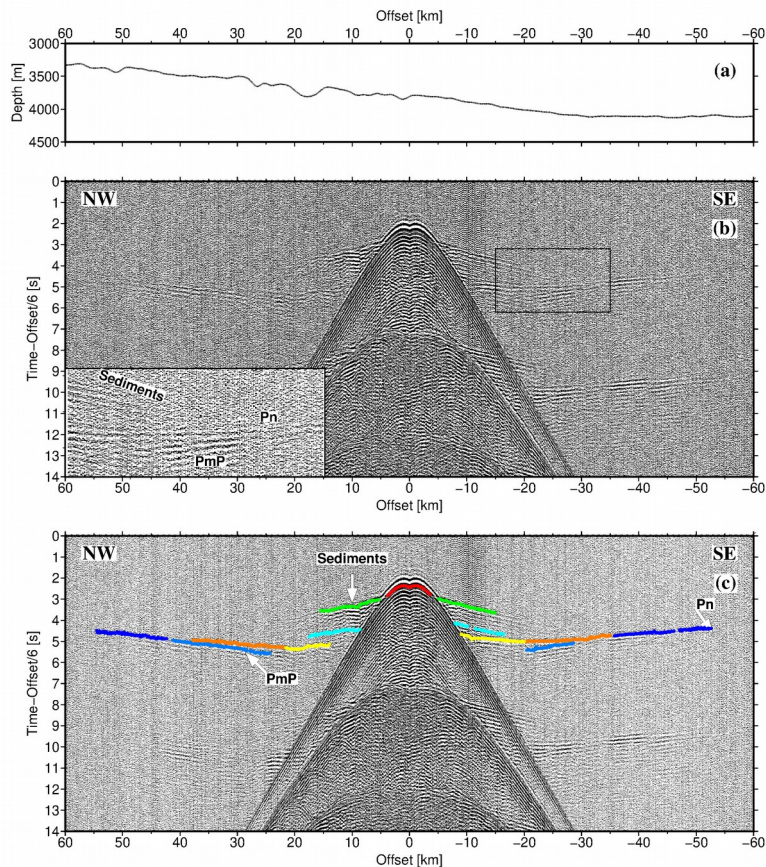
274

275 Travel-time picking was performed when possible on unfiltered data sections. When  
276 necessary a Butterworth frequency bandpass filter was used to enhance the signal/noise  
277 ratio. A total of 23971 picks were used for the velocity modeling, including 17 phases (Table  
278 1). The high number of phases is due to the lateral changes of the tectonic regime along this  
279 long profile. Although the absolute number of layers of the final velocity model is high (12  
280 layers including water surface and Moho), the number of layers at any given position along  
281 the profile never exceeds 7. The high absolute number of layers can be explained by the  
282 lateral change of character of the sediments and crust from oceanic to the accretionary  
283 wedge and the Calabria block. Along the oceanic part of the profile, within the accretionary  
284 wedge 4 sedimentary layers were modelled using reflected and turning arrivals. The second  
285 layer is characterized by a higher velocity than the underlying one, therefore inducing a  
286 velocity inversion. At the accretionary prism 4 sedimentary layers were also picked.  
287 However, since the second and third layer show no lateral continuity to the oceanic region,  
288 two additional layers were defined to avoid confusing the readers and to demonstrate that  
289 the origin of those two layers differs from the ones to the SE. Similarly two crustal layers  
290 were picked in the oceanic domain as well as in the backstop domain resulting in 4 individual  
291 layers, which however, are not continuous along the profile.

292

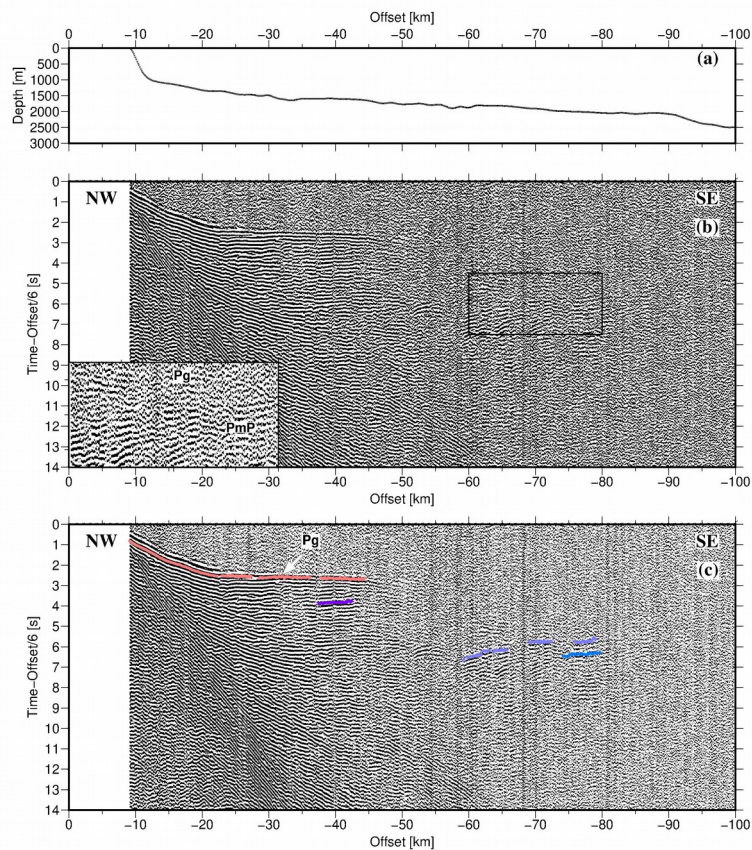
Phase	Phase Number	Number of picks	RMS error [ms]
Water	1	3879	0.030
Sediment 1	2	1133	0.129
Sediment 2	3	3616	0.079
Sediment 3	9	823	0.190
Sediment 4	18	659	0.136
Sediment 5	16	306	0.162
Sediment reflection 1	4	676	0.107
Sediment reflection 2	5	326	0.086
Sediment reflection 3	10	102	0.193
Sediment reflection 4	19	1815	0.142
Top basement	6	1469	0.178
Oceanic lower crust	15	3494	0.139
Continental lower crust	11	3039	0.147
Intra-crustal reflection	12	506	0.229
PmP continental	7	422	0.203
PmP oceanic	14	811	0.189
Pn	8	895	0.086
All phases		23971	0.133

294 Table 1: Name, phase number and RMS error for all phases.



295 Figure 3: (a) Seafloor bathymetry along the sections shown below (b) Data section from  
 296 OBS 08 vertical geophone channel. The data are bandpass filtered (3-4-24-36 Hz corner  
 297 frequencies) and reduced to a velocity of 6 km/s (c) Data section OBS 08 with travel-time  
 298 picks overlain.

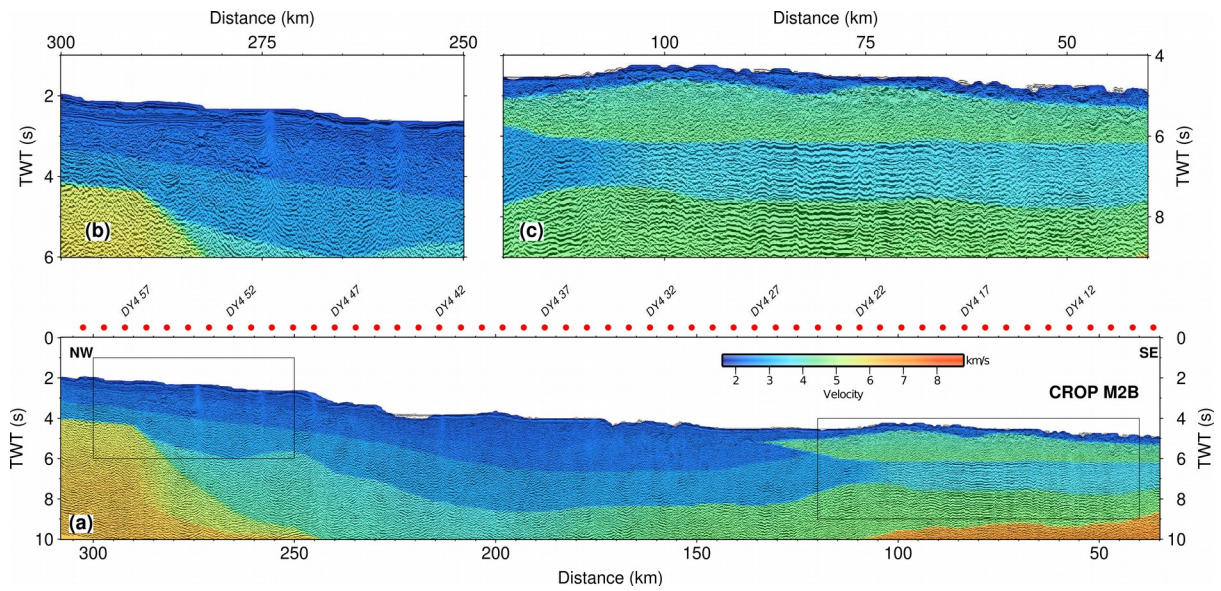




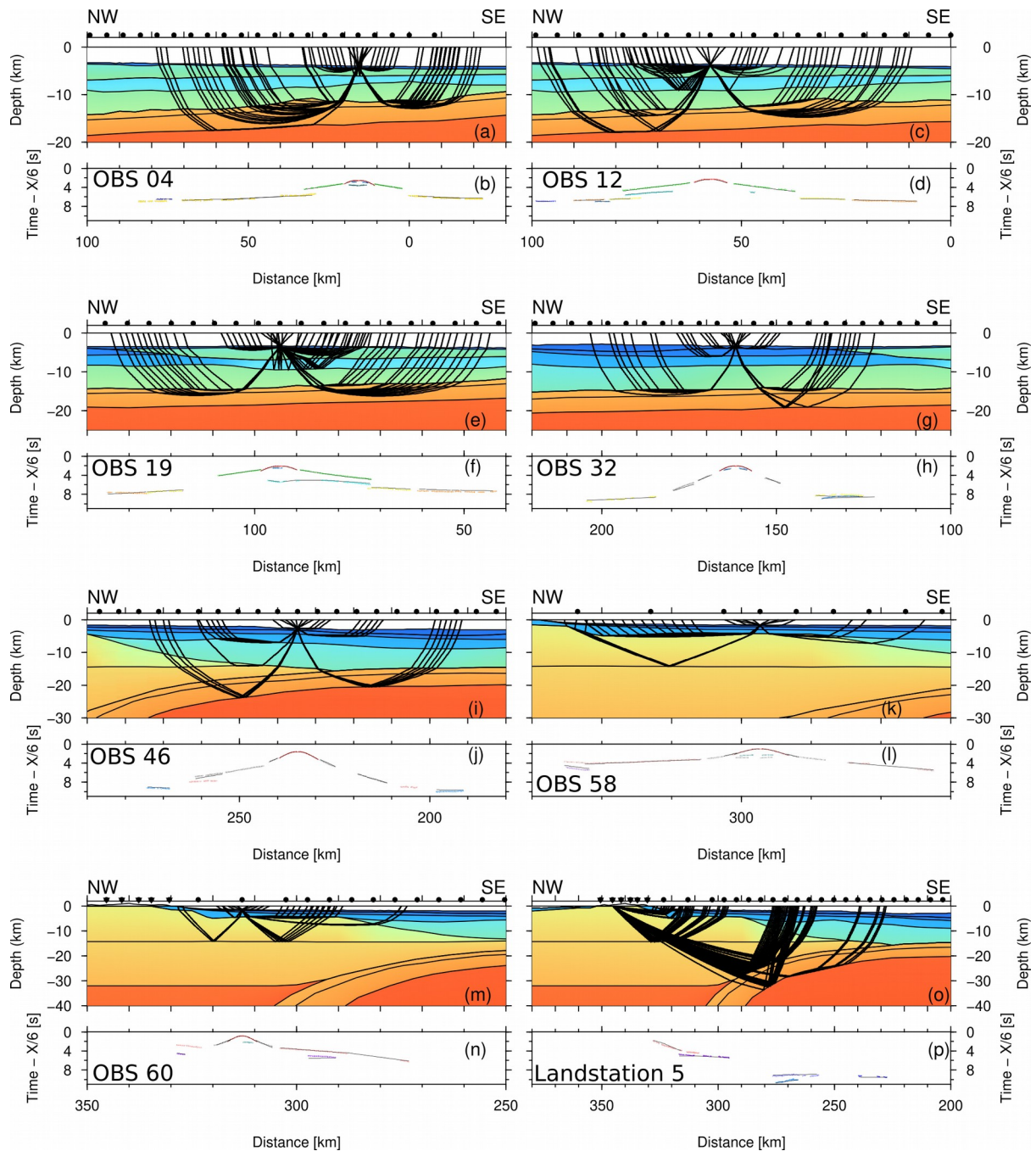
299 *Figure 4: (a) Seafloor bathymetry along the sections shown below (b) Data section from*  
 300 *landstation S3 vertical geophone channel. The data are bandpass filtered (3-4-24-36 Hz*  
 301 *corner frequencies) and reduced to a velocity of 6 km/s (c) Data section from landstation S3*  
 302 *with travel-time picks overlain.*

303

304 Key reflectors in the sedimentary layers were picked from the coincident CROP M2B time  
 305 section (Figure 5 this study and in more detail in Polonia et al., 2011) and included in the  
 306 wide-angle seismic model to better constrain the sedimentary layer geometry. The reflectors  
 307 were converted to depth with the help of the OBS data. The model was extended on land to  
 308 include the landstation data, but no reverse shots exist from the land part of the profile. The  
 309 OBS data constrain sedimentary, crustal and upper mantle parts of the model in the marine  
 310 model. The land-station data provide constraints on the deep geometry of the necking zone.  
 311 No turning wave arrivals from shallow layers on land exist as shots were only produced  
 312 along the marine part of the profile (Figure 6).



313 *Figure 5: (a) Reflection seismic section of the coincident CROP M2B profile (Polonia et al.,*  
 314 *2011) with velocities from our wide-angle seismic model underlain (see Figure 7). OBS*  
 315 *locations are marked by red circles. (b) and (c) are zooms indicated on (a) to show more*  
 316 *details of the reflection seismic data.*



318 Figure 6: Panels a,c,e,g,i,k,m,o model layers and raypaths of every 10<sup>th</sup> ray and panels b,  
 319 d,f,h,j,l,n,p corresponding travel-time picks and predicted arrivals (black lines). OBS  
 320 positions are marked in the lower panels.

## 321 2.2 Gravity modeling

322

323 To evaluate the impact of different scenarios for the slab depth along the DY-P3  
 324 profile, three different models were constructed differing only in the depth of the  
 325 slab. The first model is the (1) *reference model*, built to closely fit the predicted  
 326 free-air anomaly from the model to the measured one. Then, two end-members  
 327 models were built to test a (2) *shallow slab* hypothesis (5 km shallower slab) and  
 328 a (3) *deep slab* hypothesis (15 km deeper) (detailed explanations are given in



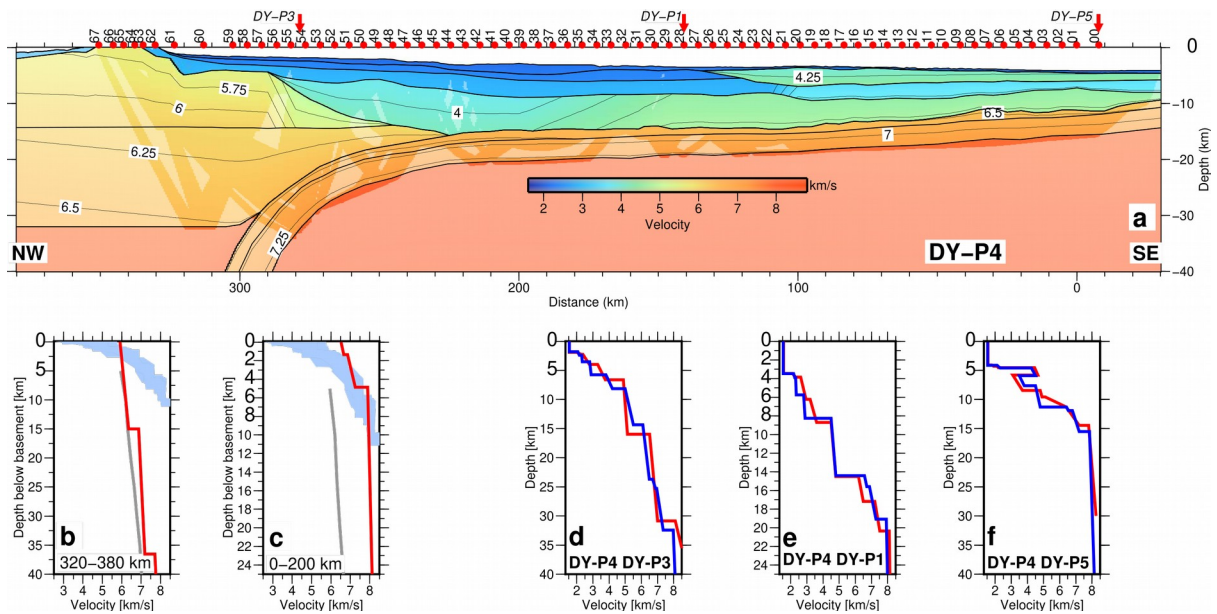
329 supplementary Text S1).

### 330 **3 Results**

331 In the following section the results from the velocity modeling are presented together with  
332 their error estimation. The results from the 3-D gravity models constructed in this study are  
333 presented thereafter.

#### 334 **3.1 Seismic velocity model**

335 The final velocity model is composed of five sedimentary units, an oceanic crustal layer  
336 subdivided into two layers (corresponding to layer 2 and 3) and a Calabrian crustal block  
337 composed of two layers (Figure 8). The deepest layer corresponds to the lithospheric  
338 mantle, however it's velocities are only constrained by diving rays in the oceanic part. The  
339 first sedimentary layer has a velocity between 2.0 and 2.3 km/s and a variable thickness  
340 between several hundreds of meters and 2-3 km. Along model distance -30 to 140 km, the  
341 second sedimentary layer is characterized by velocities between 4.5 km/s and 4.8 km/s and  
342 with a thickness between 2 and 5 km, which is characteristic for the Messinian evaporites  
343 layer located in this part of the accretionary wedge. Towards the NW this layer thickens  
344 before being pinched out by the sedimentary units of the inner part of the accretionary  
345 wedge that has lower velocities between 2.3 km/s and 2.35 km/s and a thickness of 2-3 km.  
346 The third sedimentary layer extends from the edge of the evaporite layer towards the NW  
347 with a variable thickness of ~3 km and velocities of 2.30-2.35 km/s. It was modeled as a  
348 separate layer as the velocities change abruptly from the evaporitic layer. The fourth  
349 sedimentary layer presents a lateral velocity change with higher velocities where it is  
350 underlying the evaporites of the outer accretionary wedge (3.50 – 3.80 km/s) than in the  
351 inner accretionary wedge (2.80 – 2.90 km/s). The lowermost sedimentary layer has a  
352 velocity between 4.5 km/s to 4.8 km/s in the SE and 3.8 km/s to 4.2 km/s in the NW.  
353 Together the thickness of the sedimentary cover varies between 5 km in the SW and 18 km  
354 at 230 km model distance. The Calabro-Peloritan Block is covered by only 2-3 km of  
355 sediments. The oceanic crust is 5-6 km thick with velocities increasing from 6.5-7.2 km/s to  
356 6.8-7.4 km/s towards the NW and has been subdivided into two distinct layers of  
357 approximately 2 and 4 km thickness. The Calabro-Peloritan block has a thickness of 30 km  
358 and was subdivided into two layers with velocities between 5.5 km/s and 6.6 km/s and  
359 diminishing to only 5.3 km/s at the tip of the backstop.



360 Figure 7: (a) Final velocity model of the profile DY-P4. The velocities are contoured every  
 361 0.25 km/s and shaded areas are constrained by rays. Red dots mark the position of the  
 362 seafloor instruments and arrows mark the crossing points with DY-P1 and DY-P3 profiles. (b)  
 363 and (c) Averaged velocity-depth profiles underneath the basement for the Ionian basin and  
 364 the Sicily crust. Blue envelope represents the velocity compilation for Atlantic oceanic crust  
 365 from White et al., 1992 and gray thick line the velocity compilation for extended continental  
 366 crust from Christensen and Mooney, 1995 (d), (e) and (f) Velocity depth profiles at the  
 367 crossing. Red line is the DY-P4 profile and blue lines trace the DY-P1 and DY-P3 profiles.

368

369 The MCS and the wide-angle seismic section show good agreement as the shallow  
 370 sedimentary layers as the layer geometry was picked on the migrated time section (Polonia  
 371 et al., 2011), however, MCS data offer a finer resolution of certain structures of the  
 372 subduction system (i.e. thrust faults, slope basins and inverted structures in the accretionary  
 373 wedge) than deep sounding wide-angle seismics (Polonia et al., 2011).

### 374 3.2 Error calculations

375 The error between the picked arrival time and the predicted time from forward modeling  
 376 indicates the fit of the model to the data. The number of picks and root mean square (rms)  
 377 travel-time residual for all phases are listed in Table 1. Error calculations included the  
 378 calculation of the nodes uncertainty smearing into neighboring parts of the model (spread  
 379 point function) (Figure S2 b), the resolution of the individual model nodes (Figure S2 d), and  
 380 the number of rays passing through the different layers (ray hit count) (Figure S2 b). We also  
 381 used “Vmontecarlo” software to produce a detailed analysis of the velocity uncertainties  
 382 (Loureiro et al., 2016) (Figure S3). A detailed description and resulting figures are shown in  
 383 the electronic supplement Text S2 and figures S2 and S3). Results from the error estimation  
 384 show that the sedimentary and oceanic crustal domain are well constrained by reflected and  
 385 turning rays. Here resolution is high with hit counts higher than 5000 per cell and smearing of  
 386 uncertainties is be low. Resolution is lower in the Calabrian lower crustal layer with only few  
 387 rays passing through the layer and underneath the salt layer due to the velocity inversion  
 388 from the salt to underlying sedimentary layers. The Monte Carlo inversion shows a good fit  
 389 with uncertainties not exceeding 1.0 km/s for the deepest layers.

390

391

### 392 3.3 Gravity models

393

394 In the Ionian basin, the free-air anomaly increasingly positive towards the S (Figure 8). The  
395 Apulian and Malta escarpments are characterized by strong positive free-air anomalies. In  
396 central Sicily a negative anomaly contrasts with the positive free-air anomaly of Mount Etna,  
397 the Peloritan Mountains and the Hyblean Plateau. In the Tyrrhenian basin a relatively  
398 homogeneous anomaly is observed with a value of approximately 50 mGal with the  
399 exception of the Eolian Islands presenting stronger anomalies.

400

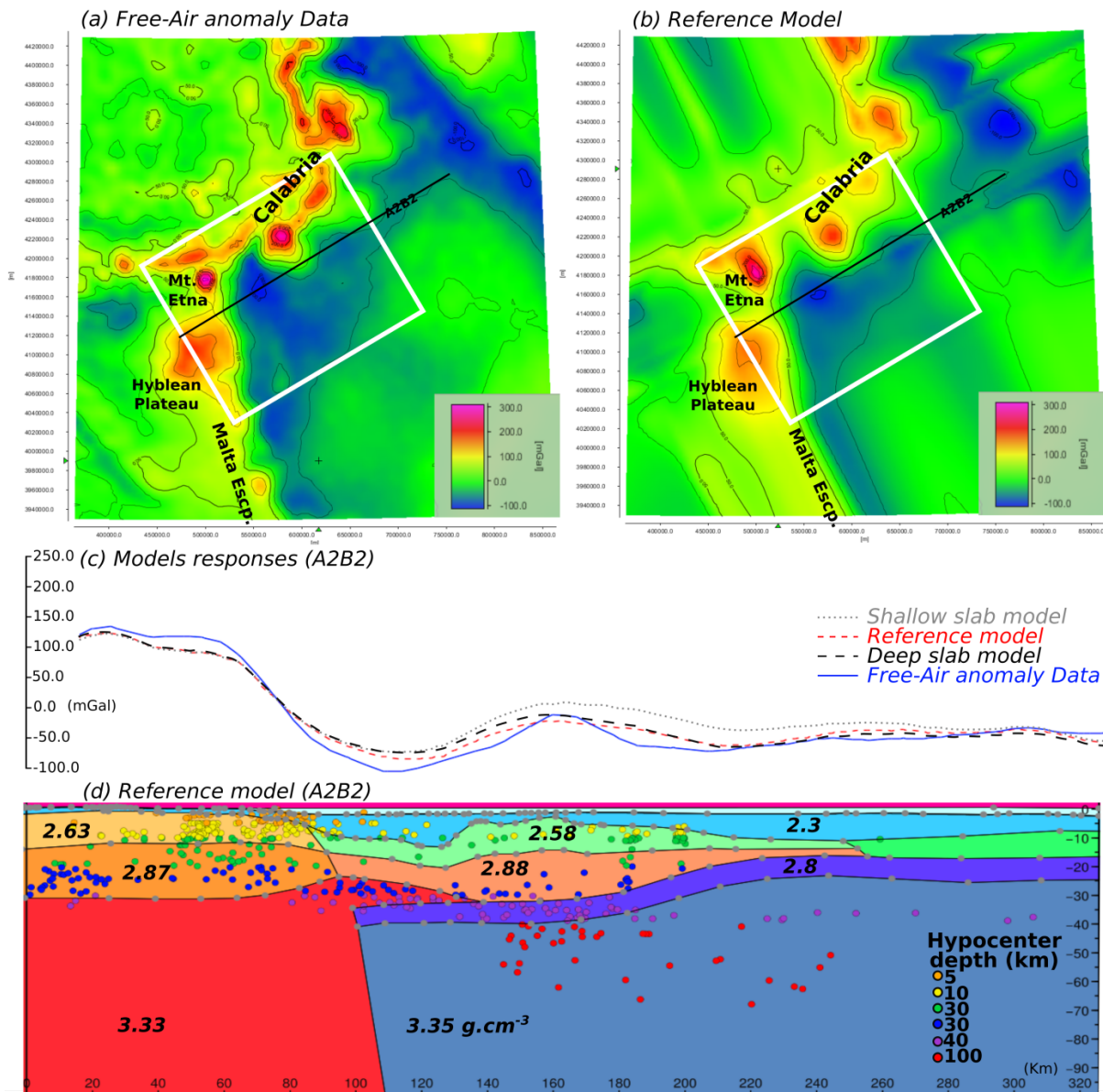
401 The 3-D gravity models were built to reproduce these main features observed in the free-air  
402 anomaly. The long wavelength features of the free-air anomaly data are well reproduced  
403 throughout the three 3D gravity models, showing that the deep density variations are  
404 explained by our models. Short wavelength variation are less well reproduced, meaning that  
405 some shallower features maybe missing in the models.

406

407 The *reference model* places the top of the oceanic crust at a depth of about 30 km along this  
408 profile comparable to the wide-angle seismic model. For the “*deep slab*” model, the top of  
409 the oceanic crust is set at a depth of about 45 km along the A2B2 cross-section. The slab  
410 then deepens to 60 km to the N-E along the GH cross-section allowing to observe the 3-D  
411 effect of a high-density body sandwiched in between the Calabrian continental crust and the  
412 oceanic crust. The calculated anomaly from this *deep slab* model increases by about 20  
413 mGal with respect to the *reference model* and also affects the resulting anomaly beyond the  
414 direct slab depth deepening zone, in an area greater than 30 km. To the N, along the GH  
415 cross-section, the slab deepening resulted in an increase of 10 mGal in the calculated  
416 anomaly in comparison to the reference model and in the S, along the ST cross-section, in  
417 an increase of less than 5 mGal.

418





419  
 420 Figure 8: (a) Map of the Free-air gravity anomaly (WGM-2012 – Bonvalot et al., 2012; Pavlis  
 421 et al., 2012) (b) 3D Reference model gravity response. White rectangle shows the area of  
 422 interest around the A2B2 profile (black line). (c) Gravity response of the different 3D models  
 423 (solely varying the oceanic slab depth) along the A2B2 profile. (d) A2B2 cross-section  
 424 extracted from the Reference model, showing each individual layers and their densities.  
 425 Earthquake hypocenters, projected from 10 km onto the profile, are shown by small circles  
 426 colored by depth.

427  
 428 For the “shallow slab” model, the oceanic crustal layer depth was decreased to 20-25 km  
 429 along the A2B2 cross-section. This configuration is a more realistic hypothesis suggested in  
 430 the past (Dellong et al., 2018). This model resulted also in an increase of the calculated  
 431 gravity anomaly with respect to the reference model. But this increase is significantly greater  
 432 than the one calculated for the “deep slab” model, and is about 30 mGal. This modification  
 433 does not affect the gravity anomaly at a large wavelength as this increase is only calculated  
 434 for the areas that are close to the modification (less than 10 km along the cross-section). To  
 435 the N (along the GH cross-section) we observed a small effect of this modification on the  
 436 gravity anomaly (less than 5 mGal). However, it is characterized by a decrease of the  
 437 anomaly in comparison to the reference model. In addition, to the S, along the ST cross-

438 section this shallow slab model shows an increase of less than 5 mGal of the calculated  
439 gravity anomaly.

440

441 Three mantle densities were used to satisfactorily fit the data. These reflect three different  
442 geodynamical origins: a continental Hyblean mantle layer derived from the wide-angle  
443 velocity models (at  $3.33 \text{ g/cm}^3$  shown in red in Figure 8 in more detail in supplementary  
444 material Figure S4 and Table S1); an oceanic mantle layer ( $3.35 \text{ g/cm}^3$ , in blue), and a back-  
445 arc mantle layer ( $3.22 \text{ g/cm}^3$ , in pink). The relative difference of these values depends on the  
446 depth of the gravity model. However from preliminary tests it is clear that models using one  
447 single density for the mantle do not allow to sufficiently fit the data. These last two layers  
448 were obtained by extrapolating the tomographic models (Scarfi et al., 2018) and therefore do  
449 not have a corresponding velocity in Table S1, which provides only velocities from wide-  
450 angle seismic modeling. The difference between the Hyblean and Tethyan oceanic mantle  
451 domains is small and can be explained by several factors, such as mantle composition or  
452 thermal state. However, the density of the Tyrrhenian mantle is significantly different as also  
453 observed in the tomographic model (Scarfi et al., 2018). This difference is probably related to  
454 the post-Messinian back-arc extension, subduction induced mantle convection, ensuing  
455 asthenospheric upwelling and associated very high heat flow (Zito et al., 2003).

456

457 2D gravity models produced using the “xgravmod” software of Colin Zelt along the profile  
458 DY04 are shown in the electronic supplements (Zelt, 1999; supplementary Text S3 and  
459 Figure S5). In this more detailed model densities from the seismic velocities the sedimentary  
460 and oceanic crustal sections and the mantle velocities from the 3D gravity modeling were  
461 taken into account. The resulting fit is high and allows to reproduce small gravity anomalies  
462 unresolved by the 3D models.

463

## 464 **4 Discussion**

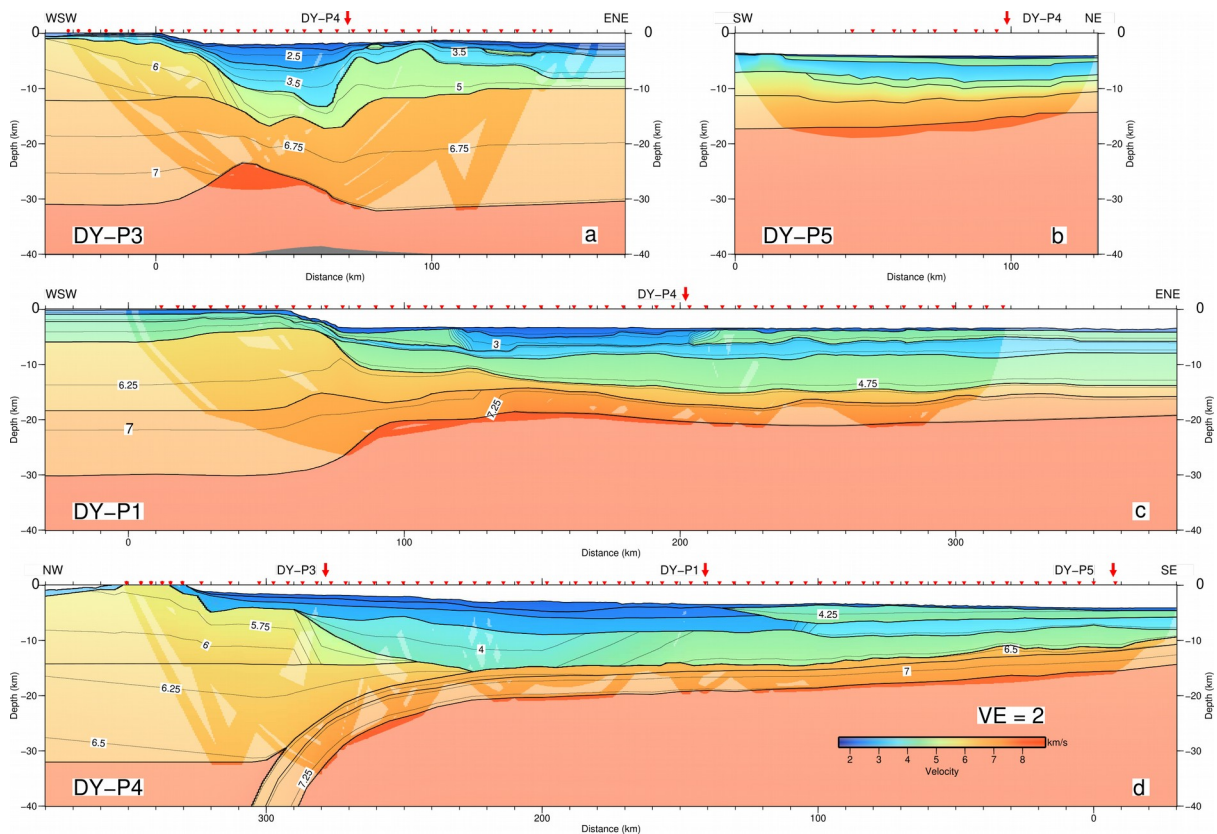
### 465 **4.1 Gravity**

466 The results obtained from the three 3-D gravity models, show that the reference model has  
467 the best fit to the free air gravity anomaly. In this reference model the top oceanic crust is  
468 located at around 25 to 30 km depth along the A2B2 cross-section (specifically along the DY-  
469 P3 velocity model). Based on the hypothesis that the recorded seismicity is predominantly  
470 intra-crustal, the corresponding slab depth is in good agreement with either the reference  
471 model and/or the shallow slab model along the DYP3 profile. The three gravity models allow  
472 us to conclude that a mantle wedge is highly unlikely to exist below the Calabrian backstop  
473 along the DY-P3 velocity profile. The models show relatively large uncertainties concerning  
474 the depth of the interfaces of  $\pm 2.5 \text{ km}$  for the Moho interface and the top of the oceanic  
475 crust. These results are in agreement with the DY-P4 velocity model and also the  
476 tomographic model from Scarfi et al., 2018. Three different lithospheric mantle densities  
477 enabled us to reproduce the large-scale regional observed free-air gravity anomaly and then  
478 test the three slab depth hypotheses. These densities were attributed to the Tethyan oceanic  
479 domain ( $3.35 \text{ g/cm}^3$ ), the mantle below the Hyblean plateau ( $3.33 \text{ g/cm}^3$ ) and the mantle of  
480 the Tyrrhenian backarc domain ( $3.22 \text{ g/cm}^3$ ), respectively. The difference between the  
481 Hyblean and Tethyan mantle domains is fairly small and can be explained by several factors,  
482 such as composition or thermal state of the mantle. However, the density of the Tyrrhenian  
483 mantle is significantly different as also observed in the tomographic model (Scarfi et al.,  
484 2018). This difference is probably related to the post-Messinian back-arc extension,  
485 asthenospheric upwelling and associated very high heat flow (Zito et al., 2003).

## 486 4.2 Velocity models

487 A comparison of the DY-P4 velocity model with the three previously published velocity  
488 models (DY-P1, DY-P3 and DY-P5) (Dellong et al., 2018; Dannowski et al., 2019) provides a  
489 3-D view of the Ionian basin (Figure 9). The fit at the crossing points is good, with slight  
490 differences that may be due to anisotropy or data quality (Figure 7 d,e,f). Sedimentary  
491 thickness in the basin is highest at the backstop contact (10-12 km). The Messinian salt  
492 layer is imaged along profiles DY-P1, DY-P4 and DY-P5 with a thickness of up to 4 km. A  
493 layer of high velocity sediments is imaged in the southern part of the basin (4.5 – 4.8 km/s).  
494 This high P-wave velocity layer, showing parallel high amplitude reflections has long been  
495 described below the IAP (Makris et al., 1986; de Voogd et al., 1992; Minelli & Faccenna,  
496 2010; Gallais et al., 2011) and likely represents Jurassic deep water carbonates, the only  
497 sedimentary rocks with such high velocities aside from halite (Anselmetti and Eberli, 1993).  
498 Oceanic crust underlying the basin is ~5 km thick, implying it is thinner than normal Atlantic  
499 ocean crust from existing compilations throughout the basin, which has a mean thickness of  
500 7.1 km (White et al., 1992). Crustal thickness increases abruptly at the Malta escarpment  
501 (DY-P1), and at the Sicily Margin (DY-P3) and the Peloritan backstop (DY-P4), indicating the  
502 presence of continental crust in these domains (Figure 9). Similarly, in both DY-P3 and DY-  
503 P4 velocity models, the upper crustal velocities increase laterally toward the continental  
504 blocks of the Sicily margin (DY-P3, from 5.0 to 6.0 km/s) and Peloritan backstop (DY-P4,  
505 from 4.75 to 5.75 km/s). These two continental domains differ in their lower crustal layers  
506 with higher velocities in the Sicily margin. While the DY-P1 and DY-P3 are imaging the same  
507 continental Sicily margin through the Malta Escarpment, profile DY-P4 images a different  
508 continental block that is likely related to Peloritan backstop, inherited from the roll-back of the  
509 Calabrian Subduction. Another discrepancy between DY-P3 and DY-P4 is the presence of  
510 the slab (Figure 7 and supplementary material Figure S6). While along DY-P3 no slab was  
511 modeled, along the profile DY-P4 the slab is clearly imaged by the data from the land-  
512 stations. This difference is due to the fact that the data quality of the land-stations along DY-  
513 P4 is very high, and from OBS data alone on DY-P3 the slab could not be detected.  
514 Furthermore, the ENS-WSW orientation of profile DY-P3 very close to and parallel to the NW  
515 dipping slab hinge was unfavorable for recording deep crustal or upper mantle arrivals, as  
516 most of the seismic energy from the airgun shots would be transmitted down dip to the NW  
517 and off profile. The Moho depth along model distance 80-120 km on profile DY-P3 (31 km)  
518 corresponds to the depth of the oceanic Moho along DY-P4, however, the backstop-slab  
519 interface was not detected along DY-P3 (Figure 9). This result is in good agreement with  
520 results from the gravity modeling. In the S DY-P4 intersects with profile DY-P5 where both  
521 profiles image thin crust interpreted to be of oceanic origin (Dannowski et al., 2019).





522 *Figure 9: Final velocity models of the wide-angle seismic profiles DY-P3 (a), DY-P5 (b), DY-*  
 523 *P1 (c) and DY-P4 (d) Crossings between profiles are marked by red arrows and OBS*  
 524 *positions by inverted triangles. Vertical exaggeration is 2.*

525

526 Comparison of these results with existing compilations of crustal thickness and Moho depth  
 527 shows a good agreement in the center of the basin (Nicolich et al., 2000), but significant  
 528 differences exist at the Sicily margin and the Malta escarpment, where the older studies  
 529 propose relatively thin crust (~24 km) compared to our data that suggest a thickness of up to  
 530 30 km. These differences are probably due to the paucity earlier, wide-angle seismic data  
 531 along these margins.

532

533 During the CAT/SCAN seismic experiment 18 land-stations were deployed to record  
 534 teleseismic events during nearly 2 years at the Sila Plateau in southern Italy. Using receiver  
 535 functions from 586 events the depth of the Ionian Moho was calculated to lie at around 35  
 536 km underneath the eastern part of Calabria gently dipping westward (Piana Agostinetti et al.,  
 537 2009). The depth increases steeply to ~80 km beneath western Calabria. This study is  
 538 located about 150 km N of DY-P4 so direct comparisons are not possible. However, the  
 539 thickness of the Calabrian crust and steep dip of the subducting crust are in good agreement  
 540 with our results. The authors also propose the existence of a 6-10 km thick layer of  
 541 underplated sediments between the Ionian and Calabrian crust, which was not imaged in our  
 542 velocity model. This might be due to the fact that our velocity model in the NW end is mainly  
 543 constrained by reflected arrivals from the land stations, which might render the detection of  
 544 low velocity zones difficult. Also this observation is based on S-wave velocities, which we  
 545 were not able to model. Another explanation might be that our profile is located at the  
 546 western edge of the subduction zone, where the crust is located at a shallower depth with  
 547 respect to the center of the arc as imaged by tomography (Maesano et al., 2017, Scarfi et  
 548 al., 2018). In central Calabria, the slab is highly arcuate and may transport a greater amount  
 549 of sediments.

### 550 **4.3 Results from earthquake tomography**

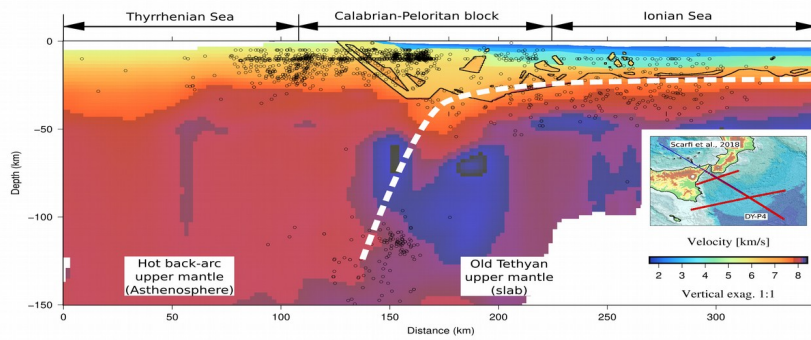
551 A detailed tomographic image of the Calabrian subduction was constructed from local  
552 earthquakes (Scarfi et al., 2018) (Figure 10). The results indicate that the slab is continuous  
553 only below the southern Calabro-Peloritan arc where its curvature is highest. In the SW,  
554 deformation at the free slab edge has led to detachment of a slab fragment and the  
555 formation of a slab window between 50 and 100 km (Scarfi et al., 2018). Comparing the  
556 wide-angle seismic velocity model, with results from the earthquake tomography and  
557 earthquake distribution, allow us to correlate the shallow layers to the deep mantle  
558 structures. The downgoing slab is continuous and steeply inclined in this region and can be  
559 traced as a high P-wave velocity anomaly as well as by using the distribution of earthquake  
560 hypocenters. The Moho depths are similar in the Ionian Basin, and in the part of the arc  
561 constrained by seismic rays. The thickness of the low velocity accretionary wedge is similar  
562 as well. The tomographic model shows that the physical properties of the mantle differ  
563 between the Ionian and the Tyrrhenian Basins, which led us to use different values for our  
564 gravity modeling. The low velocity anomaly in S-wave velocity indicated from receiver  
565 function analysis (Piana Agostinetti et al., 2009) does not correspond to a low velocity zone  
566 in P-wave velocity in the tomographic model.

567

568 Particularly interesting features of the Calabrian slab geometry as constrained by our wide-  
569 angle seismic data and the tomographic image are: the extremely shallow average dip of  
570  $1.3^\circ$  of the subducting oceanic crust over the frontal 200 km, (deepening from 11 km to  
571 about 16 km), the slab hinge where the slab dip increases abruptly from  $2-5^\circ$  to  $60-70^\circ$  over  
572 a distance of  $\leq 50$  km. By comparison with regional tomography data, only the very steep dip  
573 of the deep slab below 60 km depth (about  $70^\circ$ ) can be deduced. One of the novelties of this  
574 work is the first successful imaging using wide-angle seismic data of a slab hinge with such  
575 an extremely abrupt steepening.

576

577 Finally, the very narrow geometry of the Calabrian slab (lateral width  $\leq 200$  km) (Neri et al.,  
578 2012; Scarfi et al., 2018) may contribute to the steep dip. Indeed, numerous analogue  
579 (Funciello et al., 2006; Schellart, 2004) and numerical modeling studies (Govers & Wortel,  
580 2005) have shown that for narrow slabs, the toroidal flow around the slab is facilitated,  
581 enabling the slab to roll back more rapidly and contributing to increasing its dip (see also  
582 section 4.4 below on deep slab geometries). SKS splitting observed in the mantle below  
583 southern Italy confirm strong toroidal flow behind the Calabrian slab (Civello & Margheriti,  
584 2004). Such extremely narrow slabs (e.g. - Calabria, Gibraltar) were excluded in the global  
585 analysis of subduction zones since their segment lengths were considered too short to be  
586 representative of typical slab behavior free of edge effects (Heuret et al., 2006, Lallemand et  
587 al., 2005).



588 *Figure 10: Profile extracted from the tomographic model of (Scarfi et al. 2018) with layer*  
 589 *boundaries from the DY-P4 profile overlain. Earthquakes projected from a maximum of 5 km*  
 590 *distance along the profile are marked as black dots. P-wave velocities in the model are*  
 591 *indicated by the scale at right (in the inset). Inset: Bathymetry of the study region (Gutscher*  
 592 *et al, 2017). Blue line shows position of the tomography model and red dots OBS positions.*

593

#### 594 **4.4 Narrow curved subduction zones and deep slab structure**

595

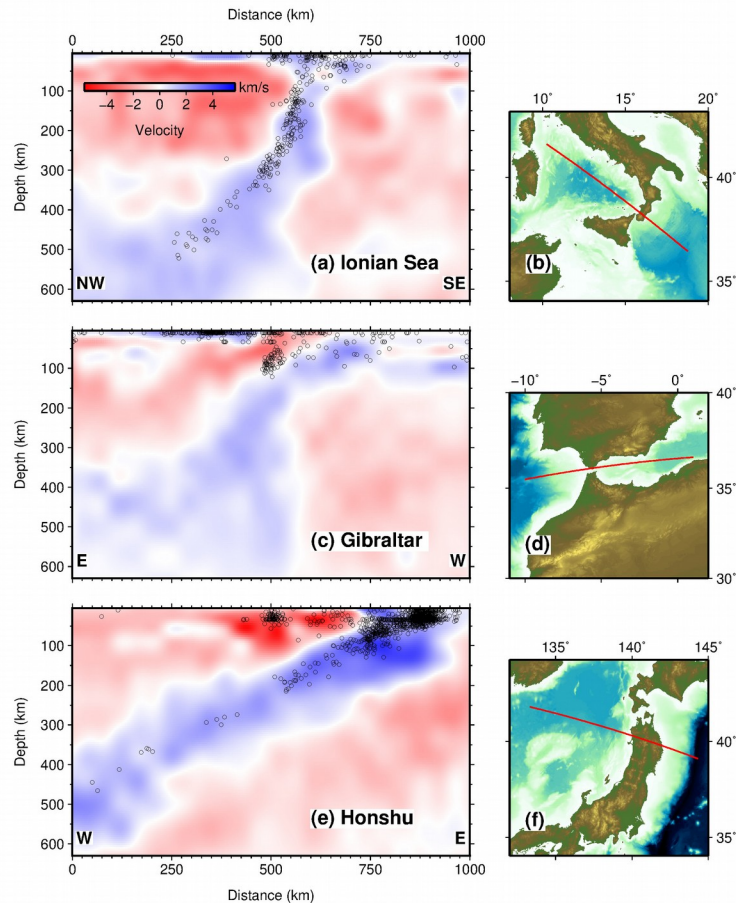
596 Global travel time tomographic images of the upper mantle reveal slab geometries at large  
 597 scale (Bijwaard et al., 1998) and can also image ongoing geodynamic processes such as  
 598 slab tearing and slab detachment (Wortel and Spakman, 2000). Here we present three  
 599 examples of deep slab geometries, two from narrow curved arcs (Gibraltar and Calabria)  
 600 and one from a much longer laterally continuous subduction zone (Northern Honshu),  
 601 unsegmented over nearly 1000 km (Figure 11). The Calabrian subduction and Gibraltar  
 602 subduction are possibly the narrowest arcs in the world, with lateral widths of  $\leq 300$  km and  
 603  $\leq 200$  km, respectively (Wortel and Spakman, 2000; Gutscher et al., 2002; Faccenna et al.,  
 604 2004; Gutscher et al., 2017). In both cases wide-angle seismic studies have concluded that  
 605 the downgoing lithosphere is most likely oceanic in nature and of Jurassic age (Sallares et  
 606 al., 2010; Dellong et al., 2018). Both subduction systems are characterized by extremely  
 607 wide ( $\sim 200$  km down-dip direction) accretionary wedge complexes, with very shallow surface  
 608 angles and thus narrow tapers (Gutscher et al., 2002; 2009; 2012; Gallais et al., 2012;  
 609 Gutscher et al., 2017; Dellong et al., 2018). There is a broad consensus that apart from their  
 610 large-scale morpho-tectonic similarities, that both subductions formed through roll-back of  
 611 narrow slabs over the past 5 - 10 million years (Gutscher et al., 2002; Faccenna et al., 2004;  
 612 Chertova et al., 2014; van Hinsbergen et al., 2014b; Gutscher et al., 2017; Palano et al.,  
 613 2017). The overall slab geometry of both systems is also largely similar. As discussed above,  
 614 the dip of the downgoing plate is very shallow below the accretionary wedge (typically  $1-5^\circ$ ).  
 615 The plate dip increases abruptly below the overriding continental fore-arc block to  $30 - 45^\circ$   
 616 where the slab reaches depths of 50 - 100 km (Figure 11 a,b). Below 100 km (for Calabria)  
 617 and below 150 km depth (for Gibraltar) the slab dip increases to  $>60^\circ$ , locally approaching a  
 618 sub-vertical geometry (Figure 11 a,b). There are also deeper sub-horizontal high p-wave  
 619 velocity anomalies between 600 km and 660 km depth, below the Betics (S Spain) and  
 620 below Corsica - Sardinia, related to the older portions of the Gibraltar and Calabrian  
 621 subductions, respectively and already discussed at length by previous authors (Wortel and  
 622 Spakman, 2000; Faccenna et al., 2004; Bezada et al., 2013; Chertova et al., 2014; van



623 Hinsbergen et al., 2014b) and which are consistent with the long-term slab roll-back  
624 kinematics which have resulted in these narrow arcs. More recent detailed tomographic work  
625 using earthquake travel time data from local seismic networks have imaged the lateral slab  
626 tears and nearby portions of detached slabs and conclude that these two systems are  
627 approaching the terminal stages of subduction (Bezada et al., 2013; Neri et al., 2009; Scarfi  
628 et al., 2018).

629 There are some differences between the tomographic images from the respective back-arc  
630 domains, however. The Calabrian back-arc (below the Tyrrhenian Sea) shows a broader  
631 stronger low p-wave velocity anomaly, than the corresponding back-arc domain from the  
632 Gibraltar subduction (below the Alboran Sea), which exhibits a thinner zone of higher  
633 temperature asthenosphere at shallower depths (50-150 km) and further in the back-arc  
634 presents a less pronounced and more heterogeneous anomaly (Figure 11 c,d). While the  
635 estimated modern day subduction velocities are very small for both subduction systems, for  
636 Calabria 3 - 5mm/yr (Palano et al., 2012; 2017), and ~5mm/yr for Gibraltar, (Koulali et al.,  
637 2011; Palano et al., 2015), it is thought that the Tyrrhenian Sea back-arc basin had two  
638 major phases of opening linked to rapid slab roll-back, inducing vigorous mantle convection  
639 (Faccenna et al., 2001). Furthermore, the larger Tyrrhenian Sea back-arc basin, evolved all  
640 the way to seafloor spreading (Marani and Trua, 2002), whereas the W Alboran basin, while  
641 highly extended, never reached seafloor spreading (Watts et al., 1993; Booth-Rea et al.,  
642 2007; Medaouri et al., 2014). A broader subducting segment (300km vs 200km), and a  
643 larger, fully developed back-arc basin both imply more vigorous convection in the  
644 asthenospheric wedge above the subducting Calabrian slab (Figure 11 a,b).

645 The N Honshu subduction (NE Japan Trench) has a very different overall slab geometry with  
646 a nearly constant shallow (50 - 150 km depth) and deeper (200 - 500 km depth) slab dip of  
647 about 30 – 35° (Figure 11 e,f). The age of the subducting lithosphere is Mesozoic, about 130  
648 Ma (Mueller et al., 1997) and therefore rather similar to the estimated age of the lithosphere  
649 subducting below Calabria or Gibraltar. It should be noted, however, that in fact there is no  
650 statistically significant correlation between the age of the subducting lithosphere and the slab  
651 dip based on a global analysis of subduction zone parameters (Lallemand et al., 2005).  
652 Other factors play a more dominant role like the nature of the upper plate (continental vs.  
653 oceanic) or the overall kinematics of the fore-arc and back-arc (extension vs. convergence)  
654 (Lallemand et al., 2005). The reasons for the constant and very modest slab dip below N  
655 Japan and extending below NE China are probably related to an anchoring of the Pacific  
656 slab at the 660 discontinuity below NE China and a stationary trench (in a Eurasia fixed  
657 reference frame) and to the large lateral width (1000 km) of the unsegmented Pacific slab,  
658 before changing its orientation at the Kurile trench. A long, laterally continuous slab favors  
659 poloidal flow, while limiting toroidal flow around the lateral slab edge and creates a very  
660 stable kinematic configuration for the large-scale slab (Schellart, 2004; Lallemand et al.,  
661 2005). Finally, there are also major differences in the overall level of seismicity in the three  
662 slabs (Figure 11 e,f). While the N Honshu slab is marked by abundant seismicity down to  
663 200 km and then scattered seismicity down to 500 km (Figure 11 c), the Calabrian slab is  
664 also marked by abundant intermediate depth seismicity down to 300 km and thereafter less  
665 abundant but still clearly marked seismicity down to 500 km (Figure 11 a). In contrast, the  
666 Gibraltar slab exhibits a cluster of intermediate depth seismicity between 60 km and 120 km  
667 depth and no deeper seismicity below (Buforn et al., 2004) (Figure 11 b). It has been  
668 suggested that this is evidence for a horizontal tear (slab detachment) occurring here (Heit et  
669 al., 2017), though an alternative explanation is the presence of extreme bending stresses as  
670 the slab abruptly steepens (Gutscher et al., 2002). Deep focus earthquakes occur below  
671 Granada (S Spain) (Buforn et al., 2011) and confirm the presence of a deep slab here  
672 interacting with the 660km discontinuity (Bezada et al., 2013).



673 *Figure 11: (a) Cross-section in the global earthquake traveltome tomographic model UU-P07*  
 674 *(Amaru, 2007) through the Ionian sea subduction zone. (b) Location map for the profile in*  
 675 *panel (a). (c) Cross-section in the UU-P07 tomographic model (Amaru, 2007) through the*  
 676 *Gibraltar subduction zone. (d) Location map for the profile in panel (c). (e) Cross-section in*  
 677 *the UU-P07 (Amaru, 2007) through the Honshu subduction zone. (f) Location map for the*  
 678 *profile in panel (e).*

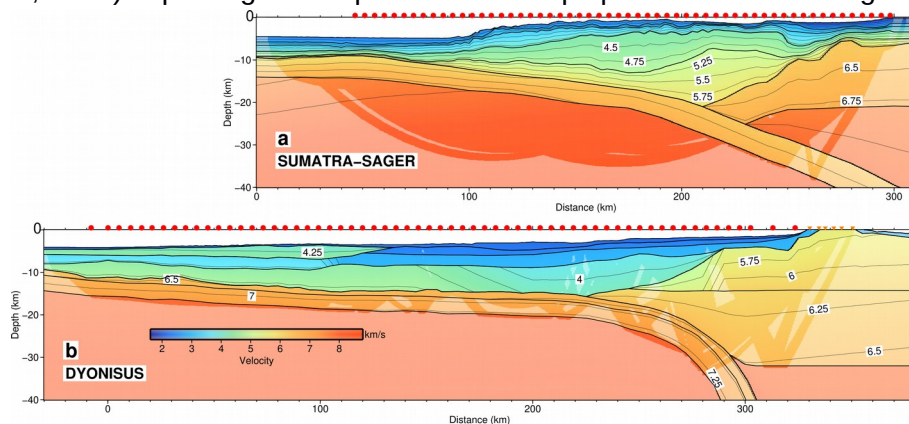
#### 679 **4.5 Comparison of two thick accretionary wedges with thick incoming** 680 **sedimentary sections**

681 If we compare the accretionary wedges from Sumatra and Calabria (Figure 12), the cross-  
 682 sectional areas of the two accretionary wedges are quite similar. For Calabria the wedge is  
 683 about 250 km wide (down-dip width) with a maximum thickness of 12-13 km and an  
 684 incoming sedimentary thickness of 5-6 km. For Sumatra, the incoming sedimentary  
 685 thickness is identical (5 km) and the width of 150 km and maximum thickness of 20 km are  
 686 40% less and 50% more than for Calabria, respectively. The main differences are the  
 687 surface slope angles which are much lower for Calabria ( $\sim 1^\circ$ ) than for Sumatra (2-3° with an  
 688 overall convex shape) and the dip of the downgoing plate. For Calabria as discussed above  
 689 it is a regular, constant  $1.3^\circ$  dip over 200 km and then the dip steepens sharply (Figure 12).  
 690 For Sumatra the dip is about  $3^\circ$  below the deformation front, and it increases progressively  
 691 to  $10^\circ$  at 20 km depth (contact with the upperplate backstop at profile km 200). The dip  
 692 remains roughly  $10^\circ$  down to 40 km depth (Figure 12 A). The overall geometry of the  
 693 Sumatra subduction resembles an ideally bulged lithosphere, with a marked 1 km high  
 694 flexural bulge visible in the wide angle seismic data (Figure 12 A, model km 50) but buried  
 695 beneath the thick Bengal Fan sediments. There would be a deep sea trench, characteristic  
 696 of most subduction zones, were it not for the enormous quantity of sediments (5 km)

697 drowning this morphological feature. The Calabrian subduction does not show this broad  
 698 scale flexure and has no flexural bulge. This may be in part due to the fact that it is a very  
 699 narrow slab and that our seismic profile is sampling the edge of the subduction zone or due  
 700 to the stiffness of the plate. In the SE and central part of the profile (Figures 11 and 12,  
 701 model km 0 - 200), the oceanic crust is still attached to the W to the continental crust of the  
 702 Hyblean domain. The slab dip increases abruptly NW of the termination of the lateral slab  
 703 tear fault (model km 280 – 300).

704

705 A second observation from this comparison is that the accretionary wedge in the Ionian  
 706 Basin is characterised by a very shallow slope in comparison to other subduction zones with  
 707 thick accretionary wedges. This fact is possibly related to the presence of Messinian  
 708 evaporites in a large part of the wedge which will facilitate sediment sliding gradually down  
 709 the slopes (Minelli & Facenna, 2010) and therefore facilitate the buildup of a large  
 710 accretionary prism. The very low taper angle of the external Calabrian Arc accretionary  
 711 wedge is comparable to that proposed for the neighbouring salt bearing Mediterranean  
 712 Ridge by Kastens (1991) through analysis of sediment facies within the wedge. Low slope  
 713 angles might be explained by the mechanical strength of the evaporites over a very weak  
 714 basal detachment that favours outward growth rather than vertical stacking of accreted units  
 715 (Polonia et al., 2011). The composition of sediments along the subducting plate and in the  
 716 accretionary prism have a direct influence on the hydrogeology, fluid budgets and  
 717 geotechnical properties of the plate-boundary (Underwood, 2007). Sediment thickness and  
 718 the lithostratigraphy of the incoming plate influence the physical properties of the margin  
 719 inducing lateral heterogeneities in the prism formation (Ike et al., 2008). Also, salt layers  
 720 influence the tectonic deformation style and spatial variation in pore water salinity resulting in  
 721 differences in fluid density and can therefore drive large scale fluid and heat transport  
 722 (Sarkar et al., 1995) impacting on the position of the updip limit of the seismogenic zone.



723 *Figure 12: Comparison of the wide-angle seismic profiles from the (a) Sumatra SAGER*  
 724 *cruise (Klingelhoefer et al., 2009) showing gradual flexure and a marked bulge expressed as*  
 725 *a basement high around 40 km profile distance and (b) DYONISUS DY-P4 showing a nearly*  
 726 *constant extremely shallow plate dip (1 – 2°) and then a slab hinge between 250 and 300*  
 727 *km profile distance where the slab dip increases abruptly to >45°.*

## 728 5 Conclusions

729 From gravity modeling we conclude that along the DY-P3 profile, the gravity model with the  
 730 oceanic slab at an intermediate depth of about 25 km shows the best fit. This model implies  
 731 that there is no mantle layer between the Calabrian backstop crust and the dipping slab. In  
 732 order to obtain a good fit to the observed gravity anomaly and with respect to the  
 733 tomographic models, the mantle densities in the Tethyan oceanic domain (3.35 g/cm<sup>3</sup>) must



734 differ substantially from those in the Tyrrhenian backarc domain (3.22 g/cm<sup>3</sup>). This is in good  
735 agreement with the fact that the basins are of different ages and with the presence of hot,  
736 convecting mantle/asthenosphere beneath the back-arc domain.

737

738 The velocity model for the DY-P4 profile images thin oceanic crust throughout the basin  
739 beneath the accretionary prism. At the NW end of the profile the Calabrian backstop extends  
740 underneath the accretionary wedge to about 100 km SE of the Calabrian coasts. The thick  
741 accretionary wedge is divided in four layers comprising a high velocity evaporitic layer and a  
742 high velocity stratified layer deposited directly on top of the oceanic basement and probably  
743 consisting of deep-water carbonates. The presence of Messinian evaporites in a large part of  
744 the wedge causing a very low basal friction facilitates lateral spreading during convergence  
745 and favors construction of a very long, shallowly tapered accretionary prism.

746

747 Prolongation of the model using earthquake hypocenters and regional tomographic data  
748 indicates that the slab dip increases abruptly from 2-3° to 60-70° over a distance of ≤50 km  
749 underneath the Calabrian backstop. This might be related to the roll-back geodynamic  
750 evolution of the narrow Calabrian slab which is similar to the Gibraltar slab showing a very  
751 comparable geometry.

## 752 **Acknowledgements**

753 We thank the captain and crew of the R/V Meteor for the data acquisition during the marine  
754 survey. The DIONYSUS cruise (M111) was funded through the Deutsche  
755 Forschungsgemeinschaft DFG. We also acknowledge Région Bretagne and Ifremer for  
756 funding the PhD scholarship associated to this work, as well as the University of Western  
757 Brittany (UBO) and the LabexMer for their help and funding of this work. We would like to  
758 acknowledge scientists and technical teams of the INGV for deploying the land-stations and  
759 Bruno Marsset from Ifremer for help processing these data. Most of the figures from this  
760 paper were generated using the Generic Mapping Tools (<http://gmt.soest.hawaii.edu>) and  
761 the Seismic Unix software was used for processing the wide-angle seismic data  
762 (<https://github.com/JohnWStockwellJr/SeisUnix/wiki>) (Cohen and Stockwell, 2003). The free  
763 OpendTect from dGB Earth Sciences (<https://www.dgbes.com/index.php/download>) and the  
764 open source Qgis software (<https://www.qgis.org/fr/site/forusers/download.html>) were used  
765 for data processing and drafting of several figures. The ocean-bottom seismometer data  
766 used in this publication are accessible in standard Segy format upon request at  
767 <http://doi.org/10.17882/52435>

## 768 **References**

- 769 Amaru, M. L. (2007). *Global travel time tomography with 3-D reference models* (Vol. 274).  
770 Utrecht University.
- 771 Amato, A., Alessandrini, B., Cimini, G., Frepoli, A., & Selvaggi, G. (1993). Active and  
772 remnant subducted slabs beneath Italy: evidence from seismic tomography and  
773 seismicity. *Annals of Geophysics*, 36(2).
- 774 Anselmetti, F.S., and Eberli, G.B., (1993). Controls on sonic velocity in carbonates. *Pure*  
775 *Appl. Geophys.*, 141, 287-323.
- 776 Argnani, A., and Bonazzi, C., (2005), Malta Escarpment fault zone offshore eastern Sicily:  
777 Plio-Quaternary tectonic evolution based on new multi-channel seismic data:  
778 *Tectonics*, v. 24, TC4009, doi:10.1029/2004TC001656.
- 779 Auffret, Y., Pelleau, P., Klingelhoefer, F., Geli, L., Crozon, J., Lin, J. Y., & Sibuet, J. C. (2004).  
780 MicrOBS: A new generation of ocean bottom seismometer. *First Break*, 22(7), 41-47.

781 Barreca, G., Scarfi, L., Cannavo, F., Koulakov, I., & Monaco, C. (2016). New structural and  
782 seismological evidence and interpretation of a lithospheric-scale shear zone at the  
783 southern edge of the Ionian subduction system (central-eastern Sicily, Italy). *Tectonics*,  
784 35, 1489–1505. doi:10.1002/2015TC004057.

785 Barreca, G., Branca, S., & Monaco, C. (2018). Three-Dimensional Modeling of Mount Etna  
786 Volcano: Volume Assessment, Trend of Eruption Rates, and Geodynamic Significance.  
787 *Tectonics*, 37(3), 842-857.

788 Bezada, M. J., E. D. Humphreys, D. R. Toomey, M. Harnafi, J. M. Davila, and J. Gallart  
789 (2013). Evidence for slab rollback in westernmost Mediterranean from improved upper  
790 mantle imaging, Spain, *Earth Planet. Sci. Lett.*, 368, 51–60,  
791 doi:10.1016/j.epsl.2013.02.024.

792 Bialas, J., & Flueh, E. R. (1999). Ocean bottom seismometers. *Sea Technol*, 40(4), 41-46.

793 Bijwaard, H., Spakman, W. and Engdahl, E.R. (1998). Closing the gap between regional and  
794 global travel time tomography. *Journal of Geophysical Research* 103, 30,055-30,078.

795 Bonvalot, S., Balmino, G., Briais, A., Kuhn, M., Peyrefitte, A., Vales, N., ... & Reinquin, F.  
796 (2012). World gravity map. *Bureau Gravimetrique International (BGI), Map, CGMW-*  
797 *BGI-CNES728, IRD, Paris.*

798 Booth-Rea, G., Ranero, C.R., Martínez-Martínez, J.M., and Grevemeyer, I. (2007). Crustal  
799 types and tertiary tectonic evolution of the Alboran sea, western Mediterranean.  
800 *Geochemistry, Geophysics, Geosystems* , v.8, doi:10.1029/2007GC001639.

801 Bouillin, J. P., Durand-Delga, M., & Olivier, P. (1986). Betic-Rifian and Tyrrhenian arcs:  
802 distinctive features, genesis and development stages. In *Developments in*  
803 *Geotectonics* (Vol. 21, pp. 281-304). Elsevier.

804 Brocher, T. M. (2005). Empirical relations between elastic wavespeeds and density in the  
805 Earth's crust. *Bulletin of the seismological Society of America*, 95(6), 2081-2092.

806 Buforn, E., M. Bezzeghoud, A. Udías, and C. Pro (2004). Seismic sources of the Iberia-  
807 African plate boundary, *Pure Appl. Geophys.* 161, 623–646.

808 Buforn, E., C. Pro, S. Cesca, A. Udías, and C. del Fresno (2011), The 2010 Granada, Spain,  
809 Deep Earthquake. *Bull. Seism. Soc. Am.*, 101, 5, 2418–2430.  
810 doi: [10.1785/0120110022](https://doi.org/10.1785/0120110022).

811 Byrne, D. E., Davis, D. M., & Sykes, L. R. (1988). Loci and maximum size of thrust  
812 earthquakes and the mechanics of the shallow region of subduction zones. *Tectonics*,  
813 7(4), 833-857.

814 Carminati, E., Negredo, A. M., Valera, J. L., & Doglioni, C. (2005). Subduction-related  
815 intermediate-depth and deep seismicity in Italy: insights from thermal and rheological  
816 modeling. *Physics of the earth and planetary interiors*, 149(1-2), 65-79.

817 Casalbore, D., Ridente, D., Bosman, A., & Chiocci, F. L. (2017). Depositional and erosional  
818 bedforms in Late Pleistocene-Holocene pro-delta deposits of the Gulf of Patti  
819 (southern Tyrrhenian margin, Italy). *Marine Geology*, 385, 216-227.

820 Catalano, R., Doglioni, C., & Merlini, S. (2001). On the mesozoic Ionian basin. *Geophysical*  
821 *Journal International*, 144(1), 49-64.

822 Cernobori, L., A. Hirn, J.H. McBride, R. Nicolich, L. Petronio, M. Romanelli, and  
823 STREAMERS/PROFILES Working Groups, 1996. Crustal image of the Ionian basin  
824 and its Calabrian margins, *Tectonophys.*, 264, 175-189.

825 Chertova, M. V., W. Spakman, T. Geenen, A. P. van den Berg, and D. J. J. van Hinsbergen,  
826 (2014). Underpinning tectonic reconstructions of the western Mediterranean region  
827 with dynamic slab evolution from 3-D numerical modeling, *J. Geophys. Res. (Solid*  
828 *Earth)*, 119, 5876–5902, doi:10.1002/2014JB011150.

829 Chiarabba, C., De Gori, P., & Speranza, F. (2008). The southern Tyrrhenian subduction  
830 zone: deep geometry, magmatism and Plio-Pleistocene evolution. *Earth and Planetary*

831 *Science Letters*, 268(3-4), 408-423.

832 Christensen, N. I., & Mooney, W. D. (1995). Seismic velocity structure and composition of  
833 the continental crust: A global view. *Journal of Geophysical Research: Solid Earth*,  
834 100(B6), 9761-9788.

835 Cimini, G. B. (1999). P-wave deep velocity structure of the Southern Tyrrhenian Subduction  
836 Zone from nonlinear teleseismic traveltome tomography. *Geophysical Research*  
837 *Letters*, 26(24), 3709-3712.

838 Civello, S., and L. Margheriti (2004), Toroidal mantle flow around the Calabrian slab (Italy)  
839 from SKS splitting, *Geophys. Res. Lett.*, 31, L10601, doi:10.1029/2004GL019607

840 Cohen, J. K., & Stockwell Jr, J. W. (2000). CWP/SU: Seismic Unix Release 35: a free  
841 package for seismic research and processing. *Centre for Wave Phenomenon*,  
842 *Colorado School of Mines*.

843 Dannowski, A., Kopp, H., Klingelhoefer, F., Klaeschen, D., Gutscher, M. A., Krabbenhoef, A.,  
844 Klaucke, I. (2019). Ionian Abyssal Plain: a window into the Tethys oceanic lithosphere.  
845 *Solid Earth*, 10(2), 447-462.

846 Dellong, D., Klingelhoefer, F., Kopp, H., Graindorge, D., Margheriti, L., Moretti, M., ... &  
847 Gutscher, M. A. (2018). Crustal Structure of the Ionian Basin and Eastern Sicily  
848 Margin: Results From a Wide-Angle Seismic Survey. *Journal of Geophysical*  
849 *Research: Solid Earth*, 123(3), 2090-2114.

850 de Voogd, B., Truffert, C., Chamot-Rooke, N., Huchon, P., Lallemand, S., & Le Pichon, X.  
851 (1992). Two-ship deep seismic soundings in the basins of the Eastern Mediterranean  
852 Sea (Pasiphae cruise). *Geophysical Journal International*, 109(3), 536-552.

853 Engdahl, E. R., van der Hilst, R., & Buland, R. (1998). Global teleseismic earthquake  
854 relocation with improved travel times and procedures for depth determination. *Bulletin*  
855 *of the Seismological Society of America*, 88(3), 722-743.

856 Faccenna, C., F. Funiciello, D. Giardini, and P. Lucente (2001). Episodic back-arc extension  
857 during restricted mantle convection in the central Mediterranean, *Earth Planet. Sci.*  
858 *Lett.*, 187, 1 - 2, 105 -116.

859 Faccenna, C., Piromallo, C., Crespo-Blanc, A., Jolivet, L., & Rossetti, F. (2004). Lateral slab  
860 deformation and the origin of the western Mediterranean arcs. *Tectonics*, 23(1).

861 Faccenna, C., P. Molin, B. Orecchio, V. Olivetti, O. Bellier, F. Funiciello, L. Minelli, C.  
862 Piromallo, and A. Billi (2011). Topography of the Calabria subduction zone (southern  
863 Italy): Clues for the origin of Mt. Etna, *Tectonics*, 30, TC1003,  
864 doi:10.1029/2010TC002694.

865 Ferranti, L., Monaco, C., Antonioli, F., Maschio, L., Kershaw, S., & Verrubbi, V. (2007). The  
866 contribution of regional uplift and coseismic slip to the vertical crustal motion in the  
867 Messina Straits, Southern Italy: evidence from raised Late Holocene shorelines.  
868 *Journal of Geophysical Research: Solid Earth*, 112(B6).

869 Forte, A. M., Dziewonski, A. M., & Woodward, R. L. (1993). Aspherical structure of the  
870 mantle, tectonic plate motions, nonhydrostatic geoid, and topography of the core-  
871 mantle boundary. *GEOPHYSICAL MONOGRAPH-AMERICAN GEOPHYSICAL*  
872 *UNION*, 72, 135-135.

873 Frizon de Lamotte, D., Raulin, C., Mouchot, N., Wrobel-Daveau, J. C., Blanpied, C., &  
874 Ringenbach, J. C. (2011). The southernmost margin of the Tethys realm during the  
875 Mesozoic and Cenozoic: Initial geometry and timing of the inversion processes.  
876 *Tectonics*, 30(3).

877 Funiciello, F., M. Moroni, C. Piromallo, C. Faccenna, A. Cenedese, and H. A. Bui (2006),  
878 Mapping mantle flow during retreating subduction: Laboratory models analyzed by  
879 feature tracking, *J. Geophys. Res.*, 111, B03402, doi:10.1029/2005JB003792.

880 Gallais, F., Gutscher, M. A., Graindorge, D., Chamot-Rooke, N., & Klaeschen, D. (2011). A



881 Miocene tectonic inversion in the Ionian Sea (central Mediterranean): Evidence from  
882 multichannel seismic data. *Journal of Geophysical Research: Solid Earth*, 116(B12).

883 Gallais, F., Gutscher, M.-A., Klaeschen, D., and Graindorge, D. (2012). Two-stage growth of  
884 the Calabrian accretionary wedge in the Ionian Sea (Central Mediterranean):  
885 Constraints from depth migrated multi-channel seismic data. *Marine Geology*, v. 326-  
886 328, p. 28-45, doi: 10.1016/j.margeo.2012.08.006.

887 Giacomuzzi, G., Civalleri, M., De Gori, P., & Chiarabba, C. (2012). A 3D Vs model of the  
888 upper mantle beneath Italy: Insight on the geodynamics of central Mediterranean.  
889 *Earth and Planetary Science Letters*, 335, 105-120.

890 Govers, R., & Wortel, M. J. R. (2005). Lithosphere tearing at STEP faults: Response to  
891 edges of subduction zones. *Earth and Planetary Science Letters*, 236(1-2), 505-523.

892 Gutscher, M.-A., Malod, J., Rehault, J.-P., Contrucci, I., Klingelhoefer, F., Mendes-Victor, L.,  
893 and Spakman, W. (2002). Evidence for active subduction beneath Gibraltar. *Geology*,  
894 v. 30, p. 1071-1074.

895 Gutscher, M.-A., Roger, J., Baptista, M.A., Miranda, J.M., and Tinti, S. (2006). The source of  
896 the 1693 Catania earthquake and tsunami (Southern Italy): New evidence from  
897 tsunami modeling of a locked subduction fault plane. *Geophysical Research Letters*, v.  
898 33, n.8, L08309 10.1029/2005GL025442.

899 Gutscher, M.-A., Dominguez, S., Westbrook, G.K., Gente, P., Babonneau, N., Mulder, T.,  
900 Gonthier, E., Bartolome, R., Luis, J, Rosas, F., Terrinha, P., and the Delila and DelSis  
901 Scientific Teams (2009). Tectonic shortening and gravitational spreading in the Gulf of  
902 Cadiz accretionary wedge: observations from multi-beam bathymetry and seismic  
903 profiling. Sp. Vol. on Submarine instabilities, *Marine and Petroleum Geology*, v. 26, p.  
904 647-659, doi:10.1016/j.marpetgeo. 2007.11.008.

905 Gutscher, M.-A., Dominguez, S., Westbrook, G., Le Roy, P., Rosas, F.M., Duarte, J.C.,  
906 Terrinha, P., Miranda, J.M., Gailler, A., Sallares, V., and Bartolome, R. (2012). The  
907 Gibraltar subduction: A decade of new geophysical data. *Tectonophysics* v. 574-575, p.  
908 72-91, doi: 10.1016/j.tecto.2012.08.038.

909 Gutscher, M.-A., Dominguez, S., Mercier de Lepinay, B., Pinheiro, L., Gallais, F.,  
910 Babonneau, N., Cattaneo, A., LeFaou, Y., Barreca, G., Micallef, A., and Rovere, M.,  
911 (2016). Tectonic expression of an active slab tear from high-resolution seismic and  
912 bathymetric data offshore Sicily (Ionian Sea). *Tectonics*, v. 35, n.1,  
913 doi:10.1002/2015TC003898.

914 Gutscher, M.-A., Kopp, H., Krastel, S., Bohrmann, G., Garlan, T., Zaragosi, S., Klaucke, I.,  
915 Wintersteller, P., Loubrieu, B., Le Faou, Y., San Pedro, L., Dominguez, S., Rovere, M.,  
916 Mercier de Lepinay, B., Ranero, C., Sallares, V. (2017). Active tectonics of the  
917 Calabrian subduction revealed by new multi-beam bathymetric data and high  
918 resolution seismic profiles in the Ionian Sea (Central Mediterranean). *Earth and  
919 Planetary Science Letters*. 461, 61-72. doi:10.1016/j.epsl.2016.12.020.

920 Handy, M. R., Schmid, S. M., Bousquet, R., Kissling, E., & Bernoulli, D. (2010). Reconciling  
921 plate-tectonic reconstructions of Alpine Tethys with the geological–geophysical record  
922 of spreading and subduction in the Alps. *Earth-Science Reviews*, 102(3-4), 121-158.

923 Heit, B., F. d. L. Mancilla, X. Yuan, J. Morales, D. Stich, Martín, R., and A. Molina-Aguilera  
924 (2017). Tearing of the mantle lithosphere along the intermediate-depth seismicity zone  
925 beneath the Gibraltar Arc: The onset of lithospheric delamination, *Geophys. Res. Lett.*,  
926 44, 4027-4035, doi:10.1002/2017GL073358.

927 Heuret, A., & Lallemand, S. (2005). Plate motions, slab dynamics and back-arc deformation.  
928 *Physics of the Earth and Planetary Interiors*, 149(1-2), 31-51.

929 Hirn, A., Nicolich, R., Gallart, J., Laigle, M., Cernobori, L., & ETNASEIS Scientific Group.  
930 (1997). Roots of Etna volcano in faults of great earthquakes. *Earth and Planetary*

931 *Science Letters*, 148(1-2), 171-191.

932 Ike, T., Moore, G. F., Kuramoto, S. I., Park, J. O., Kaneda, Y., & Taira, A. (2008). Variations in  
933 sediment thickness and type along the northern Philippine Sea Plate at the Nankai  
934 Trough. *Island Arc*, 17(3), 342-357.

935 Jacques, E., Monaco, C., Tapponnier, P., Tortorici, L., & Winter, T. (2001). Faulting and  
936 earthquake triggering during the 1783 Calabria seismic sequence. *Geophysical*  
937 *Journal International*, 147(3), 499-516.

938 Jolivet, L., Faccenna, C., Agard, P., Frizon de Lamotte, D., Menant, A., Sternai, P., &  
939 Guillocheau, F. (2015). Neo-Tethys geodynamics and mantle convection: from  
940 extension to compression in Africa and a conceptual model for obduction. *Canadian*  
941 *journal of earth sciences*, 53(11), 1190-1204.

942 Kastens, K. A. (1991). Rate of outward growth of the Mediterranean Ridge accretionary  
943 complex. *Tectonophysics*, 199(1), 25-50.

944 Klingelhoefer, F., Gutscher, M. A., Ladage, S., Dessa, J. X., Graindorge, D., Franke, D., ... &  
945 Chauhan, A. (2010). Limits of the seismogenic zone in the epicentral region of the 26  
946 December 2004 great Sumatra-Andaman earthquake: Results from seismic refraction  
947 and wide-angle reflection surveys and thermal modeling. *Journal of Geophysical*  
948 *Research: Solid Earth*, 115(B1).

949 Koulali, A., Ouazar, D., Tahayt, A., King, R.W., Vernant, P., Reilinger, R.E., McClusky, S.,  
950 Mourabit, T., Davila, J.M., Amraoui, N. (2011). New GPS constrains on active  
951 deformation along the Africa-Iberia plate boundary. *Earth Planet. Sci. Lett.* 308 (1),  
952 211–217. doi.org/10.1016/j.epsl.2011.05.048.

953 Krien, Y., & Fleitout, L. (2008). Gravity above subduction zones and forces controlling plate  
954 motions. *Journal of Geophysical Research: Solid Earth*, 113 (B9).

955 Lallemand, S., Heuret, A., & Boutelier, D. (2005). On the relationships between slab dip,  
956 back-arc stress, upper plate absolute motion, and crustal nature in subduction zones.  
957 *Geochemistry, Geophysics, Geosystems*, 6(9).

958 Le Meur, E., Virieux, J., & Podvin, P. (1997). Seismic tomography of the Gulf of Corinth: a  
959 comparison of methods.

960 Levitt, D. A., & Sandwell, D. T. (1995). Lithospheric bending at subduction zones based on  
961 depth soundings and satellite gravity. *Journal of Geophysical Research: Solid Earth*,  
962 100(B1), 379-400.

963 Loureiro, A., Afilhado, A., Matias, L., Moulin, M., & Aslanian, D. (2016). Monte Carlo  
964 approach to assess the uncertainty of wide-angle layered models: Application to the  
965 Santos Basin, Brazil. *Tectonophysics*, 683, 286-307.

966 Ludwig, W. J., Nafe, J. E., & Drake, C. L. (1970). *The Sea*, Vol. 4, Part 1.

967 Maesano, F. E., Tiberti, M. M., & Basili, R. (2017). The Calabrian Arc: three-dimensional  
968 modeling of the subduction interface. *Scientific reports*, 7(1), 8887.

969 Makris, J., Nicolich, R., & Weigel, W. (1986). A seismic study in the western Ionian Sea. In  
970 *Annales geophysicae. Series B. Terrestrial and planetary physics* (Vol. 4, No. 6, pp.  
971 665-678).

972 Marani, M. P., & Trua, T. (2002). Thermal constriction and slab tearing at the origin of a  
973 superinflated spreading ridge: Marsili volcano (Tyrrhenian Sea). *Journal of*  
974 *Geophysical Research: Solid Earth*, 107(B9), EPM-3.

975 Marotta, M. A., Spelta, E., & Rizzetto, C. (2006). Gravity signature of crustal subduction  
976 inferred from numerical modelling. *Geophysical Journal International*, 166(2), 923-938.

977 Medaouri, M., Déverchère, J., Graindorge, D., Bracene, R., Badji, R., Ouabadi, A., ... &  
978 Bendiab, F. (2014). The transition from Alboran to Algerian basins (Western  
979 Mediterranean Sea): chronostratigraphy, deep crustal structure and tectonic evolution  
980 at the rear of a narrow slab rollback system. *Journal of Geodynamics*, 77, 186-205.

981 Minelli, L., & Faccenna, C. (2010). Evolution of the Calabrian accretionary wedge (central  
982 Mediterranean). *Tectonics*, 29(4).

983 Moretti, I., & Royden, L. (1988). Deflection, gravity anomalies and tectonics of doubly  
984 subducted continental lithosphere: Adriatic and Ionian Seas. *Tectonics*, 7(4), 875-893.

985 Moscoso, E., Grevemeyer, I., Contreras-Reyes, E., Flueh, E. R., Dzierma, Y., Rabbell, W., &  
986 Thorwart, M. (2011). Revealing the deep structure and rupture plane of the 2010  
987 Maule, Chile earthquake (Mw= 8.8) using wide angle seismic data. *Earth and  
988 Planetary Science Letters*, 307(1-2), 147-155.

989 Mueller, R. D., W. R. Roest, J.-Y. Royer, L. M. Gahagan, and J. G. Sclater (1997). Digital  
990 isochrons of the world's ocean floor, *J. Geophys. Res.*, 102, 3211–3214, doi:10.1029/  
991 96JB01781.

992 Neri, G., B. Orecchio, C. Totaro, G. Falcone, and D. Presti (2009). Subduction beneath  
993 Southern Italy close the ending: Results from seismic tomography, *Seismol. Res. Lett.*,  
994 80(1), 63–70, doi:10.1785/gssrl.80.1.63.

995 Neri, G., Marotta, A. M., Orecchio, B., Presti, D., Totaro, C., Barzaghi, R., & Borghi, A.  
996 (2012). How lithospheric subduction changes along the Calabrian Arc in southern Italy:  
997 geophysical evidences. *International Journal of Earth Sciences*, 101(7), 1949-1969.

998 Nicolich, R., Laigle, M., Hirn, A., Cernobori, L., & Gallart, J. (2000). Crustal structure of the  
999 Ionian margin of Sicily: Etna volcano in the frame of regional evolution.  
1000 *Tectonophysics*, 329(1-4), 121-139.

1001 Oleskevich, D. A., Hyndman, R. D., & Wang, K. (1999). The updip and downdip limits to  
1002 great subduction earthquakes: Thermal and structural models of Cascadia, south  
1003 Alaska, SW Japan, and Chile. *Journal of Geophysical Research: Solid Earth*, 104(B7),  
1004 14965-14991.

1005 Palano, M., L. Ferranti, C. Monaco, M. Mattia, M. Aloisi, V. Bruno, F. Cannavò, and G.  
1006 Siligato (2012). GPS velocity and strain fields in Sicily and southern Calabria, Italy:  
1007 Updated geodetic constraints on tectonic block interaction in the central  
1008 Mediterranean, *J. Geophys. Res.*, 117, B07401, doi:10.1029/2012JB009254.

1009 Palano, M., Gonzalez, P.J. and Fernandez, J. (2015). The Diffuse Plate boundary of Nubia  
1010 and Iberia in the Western Mediterranean: Crustal deformation evidence for viscous  
1011 coupling and fragmented lithosphere. *Earth and Planetary Science Letters*, 430. pp.  
1012 439-447, doi:10.1016/j.epsl.2015.08.040

1013 Palano, M., C. Piromallo, and C. Chiarabba (2017). Surface imprint of toroidal flow at  
1014 retreating slab edges: The first geodetic evidence in the Calabrian subduction system,  
1015 *Geophys. Res. Lett.*, 44, doi:10.1002/ 2016GL071452.

1016 Pavlis, N. K., Holmes, S. A., Kenyon, S. C., & Factor, J. K. (2012). The development and  
1017 evaluation of the Earth Gravitational Model 2008 (EGM2008). *Journal of geophysical  
1018 research: solid earth*, 117(B4).

1019 Piana Agostinetti, N., Steckler, M. S., & Lucente, F. P. (2009). Imaging the subducted slab  
1020 under the Calabrian Arc, Italy, from receiver function analysis. *Lithosphere*, 1(3), 131-  
1021 138.

1022 Piatanesi, A., & Tinti, S. (1998). A revision of the 1693 eastern Sicily earthquake and  
1023 tsunami. *Journal of Geophysical Research: Solid Earth*, 103(B2), 2749-2758.

1024 Polonia, A., Torelli, L., Mussoni, P., Gasperini, L., Artoni, A., & Klaeschen, D. (2011). The  
1025 Calabrian Arc subduction complex in the Ionian Sea: Regional architecture, active  
1026 deformation, and seismic hazard. *Tectonics*, 30(5).

1027 Rosenbaum, G., Lister, G. S., & Duboz, C. (2002). Reconstruction of the tectonic evolution of  
1028 the western Mediterranean since the Oligocene. *Journal of the Virtual Explorer*, 8, 107-  
1029 130.

1030 Sallares, V., Gailler, A., Gutscher, M.-A., Graindorge, D., Bartolome, R., Gracia, E., Diaz, J.,



1031 and Zitellini, N. (2011). Seismic evidence for the presence of Jurassic oceanic crust in  
1032 the central Gulf of Cadiz (SW Iberia). *Earth and Planetary Science Letters*, v. 311,  
1033 p. 112-123, doi:10.1016/j.epsl.2011.09.003.

1034 Sarkar, A., Nunn, J. A., & Hanor, J. S. (1995). Free thermohaline convection beneath  
1035 allochthonous salt sheets: an agent for salt dissolution and fluid flow in Gulf Coast  
1036 sediments. *Journal of Geophysical Research: Solid Earth*, 100(B9), 18085-18092.

1037 Scarfi, L., Messina, A., & Cassisi, C. (2013). Sicily and southern Calabria focal mechanism  
1038 database: a valuable tool for local and regional stress-field determination. *Annals of  
1039 Geophysics*, 56(1), 0109.

1040 Scarfi, L., Barberi, G., Musumeci, C. & Patanè, D. (2016). Seismotectonics of northeastern  
1041 Sicily and southern Calabria (Italy): New constraints on the tectonic structures  
1042 featuring in a crucial sector for the central Mediterranean geodynamics. *Tectonics* 35,  
1043 812–832, <https://doi.org/10.1002/2015TC004022>.

1044 Scarfi, L., Barberi, G., Barreca, G., Cannavò, F., Koulakov, I., & Patanè, D. (2018). Slab  
1045 narrowing in the Central Mediterranean: the Calabro-Ionian subduction zone as  
1046 imaged by high resolution seismic tomography. *Scientific reports*, 8(1), 5178. doi:  
1047 10.1038/s41598-018-23543-8

1048 Scarpa, R. (1982). Travel-time residuals and three-dimensional velocity structure of Italy.  
1049 *pure and applied geophysics*, 120(3), 583-606.

1050 Schellart, W. P. (2004), Kinematics of subduction and subduction-induced flow in the upper  
1051 mantle, *J. Geophys. Res.*, 109, B07401, doi:10.1029/2004JB002970.

1052 Selvaggi, G., & Chiarabba, C. (1995). Seismicity and P-wave velocity image of the Southern  
1053 Tyrrhenian subduction zone. *Geophysical Journal International*, 121(3), 818-826.

1054 Séranne, M. (1999). The Gulf of Lion continental margin (NW Mediterranean) revisited by  
1055 IBS: an overview. Geological Society, London, Special Publications, 156(1), 15-36.

1056 Schmidt, S., Plonka, C., Gotze, H. J., & Lahmeyer, B. (2011). Hybrid modeling of gravity,  
1057 gravity gradients and magnetic fields. *Geophysical Prospecting*, 59(6), 1046-1051.

1058 Spakman, W., & Wortel, R. (2004). A tomographic view on western Mediterranean  
1059 geodynamics. In *The TRANSMED atlas. The Mediterranean region from crust to  
1060 mantle* (pp. 31-52). Springer, Berlin, Heidelberg.

1061 Spakman, W., van der Lee, S., & van der Hilst, R. (1993). Travel-time tomography of the  
1062 European-Mediterranean mantle down to 1400 km. *Physics of the Earth and Planetary  
1063 Interiors*, 79(1-2), 3-74.

1064 Speranza, F., Maniscalco, R., & Grasso, M. (2003). Pattern of orogenic rotations in central–  
1065 eastern Sicily: implications for the timing of spreading in the Tyrrhenian Sea. *Journal of  
1066 the Geological Society*, 160(2), 183-195.

1067 Speranza, F., L. Minelli, A. Pignatelli, and M. Chiappini (2012). The Ionian Sea: The oldest in  
1068 situ ocean fragment of the world?, *J. Geophys. Res.* 117, B12101,  
1069 doi:10.1029/2012JB009475.

1070 Underwood, M. B. (2007). Sediment inputs to subduction zones: Why lithostratigraphy and  
1071 clay mineralogy matter. The seismogenic zone of subduction thrust faults.

1072 van Hinsbergen, D. J. J., Mensink, M., Langereis, C. G., Maffione, M., Spalluto, L.,  
1073 Tropeano, M., & Sabato, L. (2014a). Did Adria rotate relative to Africa?. *Solid Earth*,  
1074 5(2), 611-629.

1075 van Hinsbergen, D. J. J., R. L. M. Vissers, and W. Spakman (2014b). Origin and  
1076 consequences of western Mediterranean subduction, rollback, and slab segmentation,  
1077 *Tectonics*, 33, 393-419, doi:10.1002/tect.20125.

1078 Watts, A. B., J. P. Platt, and P. Buhl (1993). Tectonic evolution of the Alboran Sea Basin,  
1079 *Basin Res.*, 5, 153–177, doi:10.1111/j.1365-2117.1993.tb00063.x.

1080 Westaway, R. (1993). Quaternary uplift of southern Italy. *Journal of Geophysical Research*:

- 1081 *Solid Earth*, 98(B12), 21741-21772.
- 1082 White, R. S., McKenzie, D., & O'Nions, R. K. (1992). Oceanic crustal thickness from seismic  
1083 measurements and rare earth element inversions. *Journal of Geophysical Research:*  
1084 *Solid Earth*, 97(B13), 19683-19715.
- 1085 Wortel, M. J. R., & Spakman, W. (2000). Subduction and slab detachment in the  
1086 Mediterranean-Carpathian region. *Science*, 290(5498), 1910-1917.
- 1087 Wortel, R., Govers, R., & Spakman, W. (2009). Continental collision and the STEP-wise  
1088 evolution of convergent plate boundaries: From structure to dynamics. In *Subduction*  
1089 *Zone Geodynamics* (pp. 47-59). Springer, Berlin, Heidelberg. Zelt, C. A., & Smith, R. B.  
1090 (1992). Seismic traveltimes inversion for 2-D crustal velocity structure. *Geophysical*  
1091 *journal international*, 108(1), 16-34.
- 1092 Zelt, C. A. (1999). modeling strategies and model assessment for wide-angle seismic  
1093 traveltimes data. *Geophysical Journal International*, 139(1), 183-204.
- 1094 Zelt, C. A., & Smith, R. B. (1992). Seismic traveltimes inversion for 2-D crustal velocity  
1095 structure. *Geophysical journal international*, 108(1), 16-34.
- 1096 Zito, G., Mongelli, F., De Lorenzo, S., & Doglioni, C. (2003). Heat flow and geodynamics in  
1097 the Tyrrhenian Sea. *Terra Nova*, 15(6), 425-432.